Geomech. Geophys. Geo-energ. Geo-resour. (2023) 9:68
https://doi.org/10.1007/s40948-023-00607-2

ORIGINAL ARTICLE

A new hydro-mechanical coupling constitutive model for brittle rocks considering initial compaction, hardening and softening behaviors under complex stress states

Zhi Zheng · Hao Su · Wei Wang · Zhechao Wang · Zaobao Liu · Benguo He · Guoxiong Mei

Received: 2 September 2022 / Accepted: 9 May 2023

Abstract After the excavation of underground engineering, the failure and instability of surrounding rock under hydro-mechanical coupling conditions is a common type of engineering disaster. However, the hydro-mechanical coupling mechanical characteristics of rock have not been fully revealed, and suitable models for the stability analysis of surrounding rock under hydro-mechanical coupling conditions are very scarce. Therefore, a series of triaxial compression and cyclic loading and unloading hydro-mechanical coupling tests were carried out to study the mechanical characteristics, deformation and mechanical parameters of rock under different confining pressures and pore pressures. Then, based on Biot's effective stress principle, a hydro-mechanical coupling damage constitutive model within the framework of irreversible thermodynamics was proposed to describe the initial compaction effect, pre-peak hardening and post-peak softening behaviors. The functional relationships between the proposed model key parameters (η and ζ) and the effective stress were established to characterize the pre- and post-peak nonlinear behaviors of rock. A compaction function C_{k} for the evolution of the undamaged Young's modulus in initial compaction stage was introduced to characterize the pre-peak compaction effect. A user-defined material subroutine (UMAT) was compiled in ABAQUS to numerically implemented the proposed model. The numerical simulation results are highly consistent with the test results, the proposed model can also predict the hydro-mechanical coupling characteristics of rock under untested stress levels. In addition, the yield function of the proposed model considers the influence of intermediate principal stress, which is also suitable for the simulation of hydro-mechanical coupling characteristics under true triaxial stress states.

Z. Zheng (✉) · H. Su · G. Mei
Key Laboratory of Disaster Prevention and Structural Safety of Ministry of Education, Guangxi Key Laboratory of Disaster Prevention and Engineering Safety, College of Civil Engineering and Architecture, Guangxi University, Nanning 530004, Guangxi, China
e-mail: mrzhzhi@126.com; zhengzhi@gxu.edu.cn

Z. Zheng
Key Laboratory of Geological Hazards on Three Gorges Reservoir Area (China Three Gorges University), Ministry of Education, Yichang 443002, China

Z. Zheng
State Key Laboratory of Simulation and Regulation of Water Cycle in River Basin, China Institute of Water Resources and Hydropower Research, Beijing 100038, China

W. Wang
Key Laboratory of Ministry of Education for Geomechanics and Embankment Engineering, Hohai University, Nanjing 210098, China

Z. Wang · Z. Liu · B. He
Key Laboratory of Ministry of Education on Safe Mining of Deep Metal Mines, Northeastern University, Shenyang 110819, China

Published online: 23 May 2023

Graphical abstract

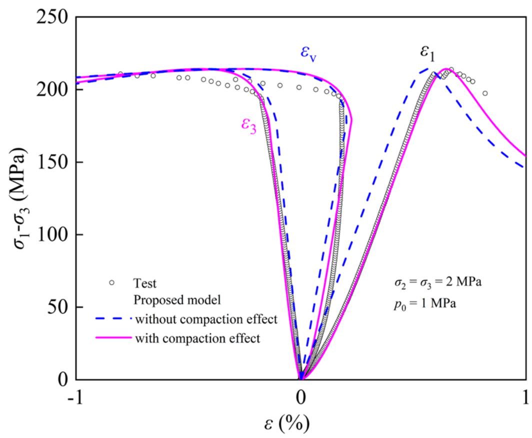

Comparison of numerical simulation results of the proposed model with and without compaction effect

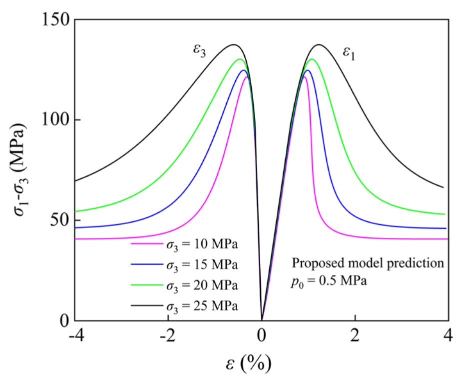

The proposed model prediction of pre-peak hardening and post-peak softening behavior characteristics of rock under different effective confining pressures

Article Highlights

- A series of triaxial compression and cyclic loading and unloading hydro-mechanical coupling tests were carried out to investigate the mechanical properties of granite gneiss under different confining pressures and pore pressures.
- A hydro-mechanical coupling damage constitutive model within the framework of irreversible thermodynamics was proposed to describe the initial compaction effect, pre-peak hardening and post-peak softening behaviors.
- The functional relationships between the proposed model key parameters (η and ζ) and the effective stress were established to better simulate the pre- and post-peak nonlinear behaviors of rock.
- A compaction function C_k for the evolution of the undamaged Young's modulus in initial compaction stage was introduced to characterize the pre-peak compaction effect.

Keywords Triaxial cyclic loading and unloading test · Hydro-mechanical · Thermodynamic damage model · Compaction effect · Rock hardening and softening · Brittle rock

List of symbols

a_1, a_2, and a_3	Characteristics parameters of η
b_1, b_2, and b_3	Characteristics parameters of ζ
b	The effective stress coefficient
B_ω	The damage evolution rate parameter
$\boldsymbol{C}_0$, $\boldsymbol{C}(\omega)$ and $\boldsymbol{C}^{\mathrm{ep}}(\gamma_{\mathrm{p}}, \omega)$	The initial elastic stiffness matrix, damage stiffness matrix and elastic−plastic tangent stiffness matrix, respectively
C_{k}	The compaction function
$d\boldsymbol{\varepsilon}$, $d\boldsymbol{\varepsilon}^{\mathrm{e}}$ and $d\boldsymbol{\varepsilon}^{\mathrm{p}}$	The total strain increment tensor, elastic strain increment tensor and plastic strain increment tensor, respectively
$d\lambda_{\mathrm{p}}$	The plastic multiplier
$d\boldsymbol{\sigma}$	The stress increment tensor
$d\boldsymbol{\sigma}'$	The effective stress increment tensor
$\boldsymbol{e}^{\mathrm{p}}$	The plastic deviatoric strain tensor
E_0 and E	The Young's modulus of undamaged and damaged material, respectively
f_{d}, f_{p} and g	The damage evolution function, yield function and plastic potential function, respectively
h	The function of hardening and softening
h_0 and h_1	The initial value and final value of h, respectively
$\boldsymbol{I}$	The fourth-order unit tensor
$\boldsymbol{J}$	The fourth-order tensor
I_1'	The first invariant of effective stress
J_2'	The second invariant of effective deviatoric stress
$k(\omega)$	The bulk modulus of damaged materials
m	The parameter of compaction coefficient
p_0	The pore pressure
Y_{d}, Y_{e}, Y_{p}	The thermodynamic forces
α, κ	The strength parameters of Drucker−Prager yield function
α_{g}	The strength parameters of plastic potential function
γ_{p}	The equivalent plastic shear strain
$\boldsymbol{\delta}$	The second-order unit tensor
ε_1, ε_2 and ε_3	The maximum, intermediate and minimum principal strains, respectively
$\boldsymbol{\varepsilon}$, $\boldsymbol{\varepsilon}^{\mathrm{e}}$ and $\boldsymbol{\varepsilon}^{\mathrm{p}}$	The total strain tensor, elastic strain tensor and plastic strain tensor, respectively
ε_{y}, ε_{p} and ε_{r}	Corresponding strain of the initial yield strength, peak strength and residual strength, respectively
$\boldsymbol{\zeta}$	The softening characteristic parameter
η	The hardening rate parameter
$\mu(\omega)$	The shear modulus of damaged materials
σ_1, σ_2 and σ_3	The maximum, intermediate and minimum principal stresses, respectively
σ_1', σ_2' and σ_3'	The maximum, intermediate and minimum principal effective stresses, respectively
σ_{y}, σ_{p} and σ_{r}	The initial yield strength, peak strength and residual strength, respectively
ψ	The thermodynamic potential
ψ_{e} and ψ_{p}	The elastic part and plastic part of thermodynamic potential, respectively
ω *and* ω_{c}	The damage variable and the damage threshold, respectively

$\Delta\boldsymbol{\sigma}'$ and $\Delta\gamma_{\mathrm{p}}$	Small increment of effective stress tensor and equivalent plastic shear strain between two steps
$\Delta 2\lambda$	The plastic multiplier increment

1 Introduction

The hydro-mechanical coupling effect is a front and difficult issue of rock mechanics and engineering (Braun et al. 2019; Khadijeh et al. 2022). The excavation of offshore and marine geotechnical engineering, water conservancy and hydropower engineering, underground energy engineering and underground transportation engineering all have potential hydro-mechanical coupling damage and disaster risk (Bernabe 1986; Rutqvist and Stephansson 2003; Guayacán-Carrillo et al. 2017; Fang and Wu 2022). There are abundant initial micropores and microcracks in engineering rock, which provide seepage channels for groundwater. Under the hydro-mechanical coupling conditions, the permeability, strength, pre-peak hardening and post-peak softening characteristics of rock are very complex (Biot 1956; Katz and Thompson 1986; Caine et al. 1996; Rutqvist et al. 2002; Zhou et al. 2019; Li et al. 2021). Especially similar to underground water-sealed oil storage caverns, the stress field and pore pressure field of surrounding rock are coupled during the construction period, and with the oil outlet and inlet process during the operation period, the surrounding rock of the storage cavern undergoes stress cyclic loading and unloading in hydro-mechanical coupling environment (Mitchell and Faulkner 2008; Xiao et al. 2021; Lyakhovsky et al. 2022). The mechanical properties of rock under complex hydro-mechanical coupling states have not been fully revealed, and the suitable hydro-mechanical coupling models are very scarce to provide theoretical guidance for engineering support, excavation design and safe operation. Therefore, it is urgent to carry out in-depth research.

Triaxial compression and cyclic loading and unloading hydro-mechanical coupling tests for rock have achieved some research results (Wang and Park 2002; Tenthorey et al. 2003; Zhang et al. 2013; Zhang et al. 2020). Previous studies have shown that confining pressure, pore pressure and stress path have significant effects on rock mechanical behaviors (including strength, pre-peak hardening, post-peak softening) and permeability (Barton 2002; Mitchell and Faulkner 2008; Zheng et al. 2019, 2022a, 2023a). Some studies have focused on the influence of pore pressure on rock strength and Young's modulus (Yu et al. 2020; Zhang et al. 2021; Zheng et al. 2022b, 2022c). According to the effective stress principle, the coupling effect of mechanical pressure and pore pressure can be expressed by the effective stress (Zheng et al. 2015; Liu et al. 2018, 2022), and the strength of rock under hydro-mechanical coupling conditions is closely related to effective stress, which increases with increasing effective stress. Some studies have focused on the mechanism of permeability evolution under hydro-mechanical coupling conditions (Zhang 2013; Tian et al. 2019; Zheng et al. 2022d); other studies have focused on the influence of the scale effect on rock permeability (Yang et al. 2017; Putilov et al. 2022); and some scholars have also studied the effects of stress paths such as loading, unloading and loading unloading on the hydro-mechanical coupling characteristics of rock (Shi et al. 2017; Ning et al. 2022). A small number of studies have focused on the progressive failure process, pre-peak hardening and post-peak softening characteristics of rock under hydro-mechanical coupling conditions (Wang et al. 2020; Kou et al. 2021; Zheng et al. 2022e). However, previous studies have mainly focused on high permeability rocks and less on low permeability brittle rocks (such as granite), and the influence of different confining pressures, pore pressures and stress paths needs further study.

The strength of rock is generally considered to be closely related to confining pressure, and many scholars have proposed some strength criteria by analyzing the relationship between strength and confining pressure, such as the Mohr−Coulomb, Drucker−Prager and Hoek−Brown strength criteria (Alejano and Bobet 2012; Si et al. 2019; Hoek and Brown 2019; Xia et al. 2022; Zheng et al. 2023b). Based on these strength criteria, some scholars have proposed hydro-mechanical coupling constitutive models to describe the strength characteristics of rock under hydro-mechanical coupling conditions and have achieved good results (Yang et al. 2018; Wang et al. 2020; Wen et al. 2022). In addition, the deformation and failure processes are the important research issues in the study of rock under hydro-mechanical coupling conditions. To characterize the hydro-mechanical coupling deformation and failure processes of rock, some rock hydro-mechanical coupling models have been proposed, which are mainly divided into five types (Nakshatrala et al. 2018; Wang et al. 2018; Liu et al. 2021b; Rueda et al. 2021; Wu et al. 2022): equivalent continuous model, discrete fracture network model, dual-porosity media model, fracture mechanical model and damage mechanical model. The equivalent continuous model reconstructs the constitutive relation and related parameters of a fractured rock mass through the theory of continuum mechanics, which avoids the difficulty of solving discontinuous problems (Laghaei et al. 2018). The discrete fracture network (DFN) model assumes that the permeability of intact rock mass is much smaller than that of fractures, and the seepage in rock mass only exists in fractures. This model can accurately characterize the small-scale hydro-mechanical coupling characteristics of fractured rock masses (Giuffrida et al. 2019). The dual-porosity media model assumes that the rock mass is composed of pores with water storage properties and fractures with water transmission properties, and the pores and fractures are independent and interconnected. To some extent, the dual-porosity media model can better simulate the seepage problem in complex media (Zhao and Chen 2006; Zhao et al. 2021). The first three models mainly involve the classical elastic−plastic theory and do not involve the damage and deterioration of the rock mass. The latter two models focus on the more complex coupling effects caused by rock damage and deterioration. Some scholars have proposed hydro-mechanical coupling models from the perspective of micromechanics and macromechanics based on the concepts of fracture mechanics and damage mechanics (Hamiel et al. 2004; Liu et al. 2021a; Xi et al. 2022; Zheng et al. 2023c). Micromechanics explains the inelastic behavior of materials from the perspective of crack propagation and friction sliding, and yet the complexity of the description method of inelastic behavior leads to a complex form of the micromechanics model, which is difficult to numerically implemented and difficult to apply in engineering (Shao and Rudnicki 2000; Zhu and Tang 2004; Jia et al. 2021); macromechanics defines internal variables to describe the plasticity and deterioration behaviors of materials, and the established phenomenological models have a simpler form and can be easily implemented in engineering applications based on finite element methods (Zhou et al. 2001; Zhao et al. 2019; Shen et al. 2022). However, the above models do not consider the post-peak softening behavior due to rock degradation. In addition, there are magnanimous initial micropores and microcracks inside the rock. These micropores and microcracks will be compacted in the initial compaction stage of rock (Baud et al. 2000; Cai et al. 2004; Zhu et al. 2022), and the corresponding stress–strain curve appears as a concave curve with increasing Young's modulus. There are few studies on the model of initial nonlinear behavior, and most of the previous models do not consider this pre-peak compaction effect (Wang et al. 2021; Hu et al. 2022), resulting in a large strain difference between the numerical simulation results and the test results. A hydro-mechanical coupling damage model considering the pre-peak compaction effect and post-peak softening effects has not been established.

In view of the aforementioned research deficiencies, a series of triaxial compression and cyclic loading and unloading hydro-mechanical coupling tests were carried out to study the mechanical characteristics, deformation and mechanical parameters of rock under different confining pressures and pore pressures. By analyzing the test results, a hydro-mechanical coupling damage model considering the compaction effect, pre-peak hardening and post-peak softening nonlinear behaviors was established within the framework of irreversible thermodynamics based on the effective stress principle. A user-defined material subroutine (UMAT) was compiled in the Fortran language, and the numerical program of the proposed model was implemented in the finite element software ABAQUS. A sensitivity analysis of the key parameters (η and ζ) of the proposed model was carried out, and the proposed model was verified with the test results. The hydro-mechanical coupling characteristics of the rock were predicted.

2 Hydro-mechanical coupling test of granite gneiss

2.1 Specimen and apparatus

The test sample is granite gneiss from a 100 m underground area obtained by core drilling in a China

(a) (b)

Fig. 1 **a** Typical granite gneiss specimen; **b** hydro-mechanical coupling test apparatus

groundwater-sealed oil cavern reservoir project. The porosity of the sample is low, there are no visible cracks, and the surface is dark black with certain white spots. According to the method recommended by the International Society of Rock Mechanics and Engineering (ISRM) (Fairhurst and Hudson 1999; Feng et al. 2019), the sample is processed into a cylinder with a diameter of 50 mm and a height of 100 mm. A typical specimen is shown in Fig. 1a.

The test system is a fully automatic triaxial microservo hydro-mechanical coupling test apparatus for rock, as shown in Fig. 1b. The test system is composed of a triaxial pressure chamber, pressurization system, computer control system, constant pressure stabilizing device, water pressure control system and automatic information acquisition system. Conventional triaxial tests, triaxial cyclic loading and unloading hydro-mechanical coupling tests of rock can be conducted. The test system can apply the maximum axial pressure, the maximum confining pressure and the maximum pore pressure of 500 MPa, 60 MPa and 30 MPa, respectively, and realize the automatic compensation of axial pressure, confining pressure and pore pressure during the loading process, with an accuracy of ±0.1 MPa. Axial strain and circumferential strain can be measured by the linear variable differential transformer (LVDT) and circumferential strain measuring ring. In the process of the hydro-mechanical coupling test, the automatic acquisition system can record the test data in real time and realize digital graph.

2.2 Stress path of the conventional triaxial hydro-mechanical coupling test

As the oil storage cavern undergoes the process of oil inlet and outlet, under cyclic loading and unloading conditions, the deformation and stability of the surrounding rock may be affected. To study the strength, deformation and failure characteristics of rock during this loading and unloading process, triaxial cyclic loading and unloading tests are needed. Since the strength of triaxial cyclic loading

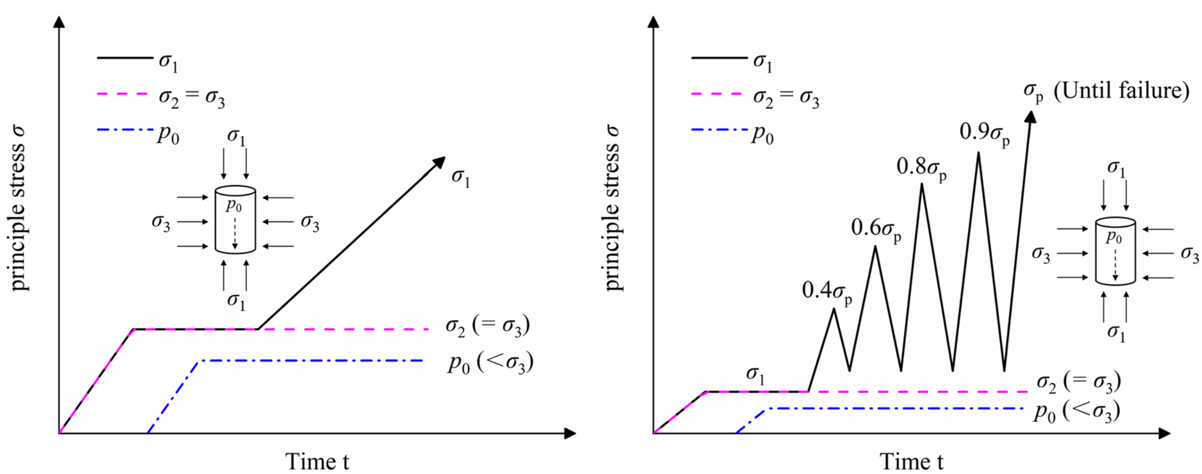

(a) (b)

Fig. 2 Stress path. **a** For conventional triaxial hydro-mechanical coupling test; **b** for triaxial cyclic loading and unloading hydro-mechanical coupling test. (p_0 is pore pressure, σ_p is peak strength) and unloading tests under different confining pressures cannot be determined, conventional triaxial tests can be conducted in advance to determine the strength of rock under different confining pressures, which provides a basis for the design of triaxial cyclic loading and unloading test processes.

Combined with the geological investigation report and the stress conditions in the sampling area of the test samples (water sealed oil storage project buried depth of approximately 100 m), confining pressures of 2 MPa, 4 MPa and 6 MPa were selected for the conventional triaxial hydro-mechanical coupling test. According to the field water level monitoring data, the pore pressure is about 1 MPa, considering excavation excess pore pressure effect, the pore pressure is set to 1, 2, 3 MPa. To meet engineering practice, all samples should be saturated for at least 4 h at a negative pressure of 0.098 MPa before the test. The test loading process is controlled by stress, and the stress path is shown in Fig. 2a:

1. Apply stress to set confining pressure σ_3 and keep confining pressure stable;
2. Apply pore pressure p_0 ($<\sigma_3$) to a set value and keep pore pressure stable;
3. Saturate the specimen until water flows out of the outlet;
4. The deviatoric stress is applied at a rate of 0.75 MPa/min until the specimen is destroyed.

2.3 Stress path of triaxial cyclic loading and unloading hydro-mechanical coupling test

According to the peak strength σ_p obtained from the conventional triaxial hydro-mechanical coupling test under different confining pressures, confining pressures of 2 MPa, 4 MPa and 6 MPa and a pore pressure of 1 MPa were selected to carry out the triaxial cyclic loading and unloading hydro-mechanical coupling test. Similarly, before the test, all the specimens were saturated for at least 4 h at a negative pressure of 0.098 MPa. The loading and unloading rate during the test process is 0.75 MPa/min, and the stress path is shown in Fig. 2b:

1. Apply stress to set confining pressure σ_3, and keep confining pressure stable;
2. Apply pore pressure p_0 ($<\sigma_3$) to set value and keep pore pressure stable;
3. Saturate the specimen until water flows out of the outlet;
4. The deviatoric stress is loaded to $0.4\sigma_p$ and then unloaded to $0.2\sigma_p$;
5. The deviatoric stress is loaded to $0.6\sigma_p$ and then unloaded to $0.2\sigma_p$;
6. The deviatoric stress is loaded to $0.8\sigma_p$ and then unloaded to $0.2\sigma_p$;
7. The deviatoric stress is loaded to $0.9\sigma_p$ and then unloaded to $0.2\sigma_p$;
8. The deviatoric stress is loaded to σ_p; if the specimen is still not destroyed, then similarly continue to load to failure.

3 Test results and analysis

3.1 Stress–strain curve characteristics of granite gneiss under hydro-mechanical coupling conditions

3.1.1 Stress–strain curve of granite gneiss under triaxial hydro-mechanical coupling test

The stress–strain curves of granite gneiss under different confining pressures and pore pressures are shown in Fig. 3. (1) In Fig. 3a–c, the constant pore pressure is $p_0 = 1$ MPa, and the confining pressures are $\sigma_3 = 2$, 4, 6 MPa; (2) in Fig. 3b, d, e, the constant confining pressure is $\sigma_3 = 4$ MPa, and the pore pressures are $p_0 = 1$, 2, 3 MPa. When pore pressure is 1 MPa and confining pressure are 2, 4, 6 MPa, the strength of rock increases with increasing confining pressure, and the strain corresponding to the peak strength of rock also increases with increasing confining pressure. When confining pressure is 4 MPa and pore pressure are 1, 2, 3 MPa, the strength of rock decreases with increasing pore pressure.

According to the shape of the stress–strain curve, it can be divided into three typical stages before the peak strength: compaction stage, linear elastic stage and hardening stage. During the initial loading process of rock, the initial micropores and microcracks are compacted, resulting in an increase in rock stiffness, which shows a concave curve in the compaction stage of the stress–strain curve. After the compaction stage, rock enters the linear elastic stage. At

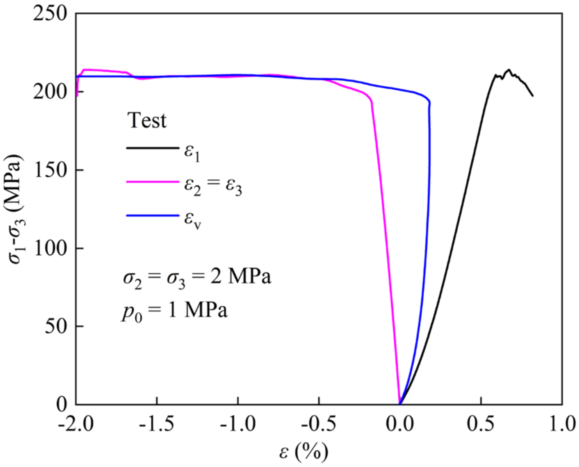

Test
ε_1
$\varepsilon_2 = \varepsilon_3$
ε_v
$\sigma_2 = \sigma_3 = 2$ MPa
$p_0 = 1$ MPa
σ_1-σ_3 (MPa)
ε (%)

(a)

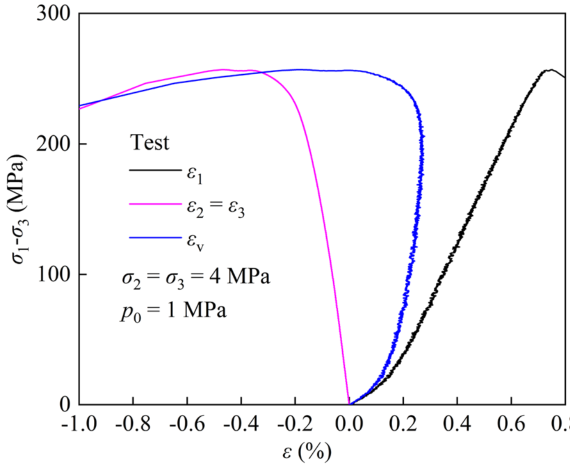

Test
ε_1
$\varepsilon_2 = \varepsilon_3$
ε_v
$\sigma_2 = \sigma_3 = 4$ MPa
$p_0 = 1$ MPa
σ_1-σ_3 (MPa)
ε (%)

(b)

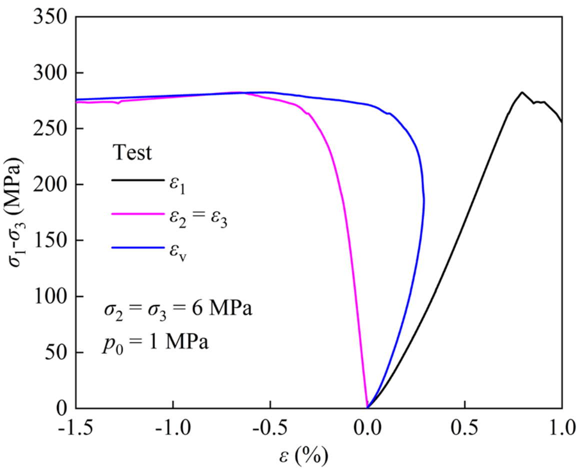

Test
ε_1
$\varepsilon_2 = \varepsilon_3$
ε_v
$\sigma_2 = \sigma_3 = 6$ MPa
$p_0 = 1$ MPa
σ_1-σ_3 (MPa)
ε (%)

(c)

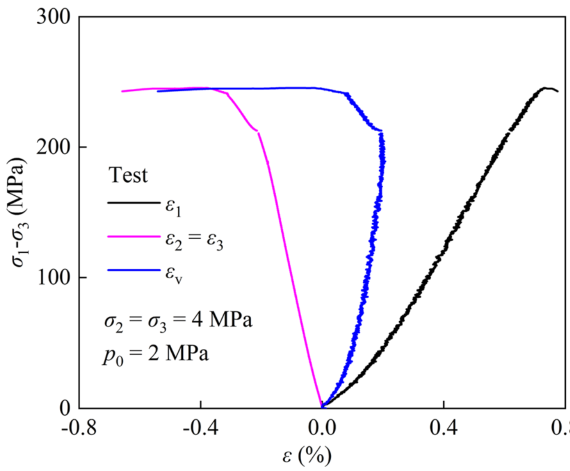

Test
ε_1
$\varepsilon_2 = \varepsilon_3$
ε_v
$\sigma_2 = \sigma_3 = 4$ MPa
$p_0 = 2$ MPa
σ_1-σ_3 (MPa)
ε (%)

(d)

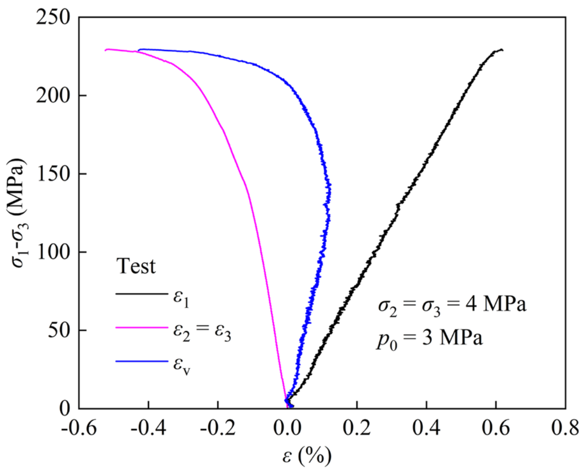

Test
ε_1
$\varepsilon_2 = \varepsilon_3$
ε_v
$\sigma_2 = \sigma_3 = 4$ MPa
$p_0 = 3$ MPa
σ_1-σ_3 (MPa)
ε (%)

(e)

◂**Fig. 3** The stress–strain curves of granite gneiss under conventional triaxial hydro-mechanical coupling test. **a** $p_0=1$ MPa, $\sigma_3=2$ MPa; **b** $p_0=1$ MPa, $\sigma_3=4$ MPa, **c** $p_0=1$ MPa, $\sigma_3=6$ MPa; **d** $p_0=2$ MPa, $\sigma_3=4$ MPa; **e** $p_0=3$ MPa, $\sigma_3=4$ MPa

this stage, the micropores and microcracks of rock is almost completely closed, and the stiffness of rock is no longer increased, showing a linear increase of stress–strain curve. Under the action of continuous loading, rock enters the hardening stage. At this stage, new cracks are increasing, and the stress–strain curve begins to show nonlinear characteristics. In addition, the variation trend of the volumetric strain curve of granitic gneiss in the compaction stage and linear elastic stage is consistent with that of the ε_1 strain. With the continuous loading of stress, the volume deformation of rock changes from compression to expansion, and the volume strain curve begins to turn.

3.1.2 *Stress–strain curve of granite gneiss under triaxial cyclic loading and unloading hydro-mechanical coupling test*

The stress–strain curves of granite gneiss under triaxial cyclic loading and unloading hydro-mechanical

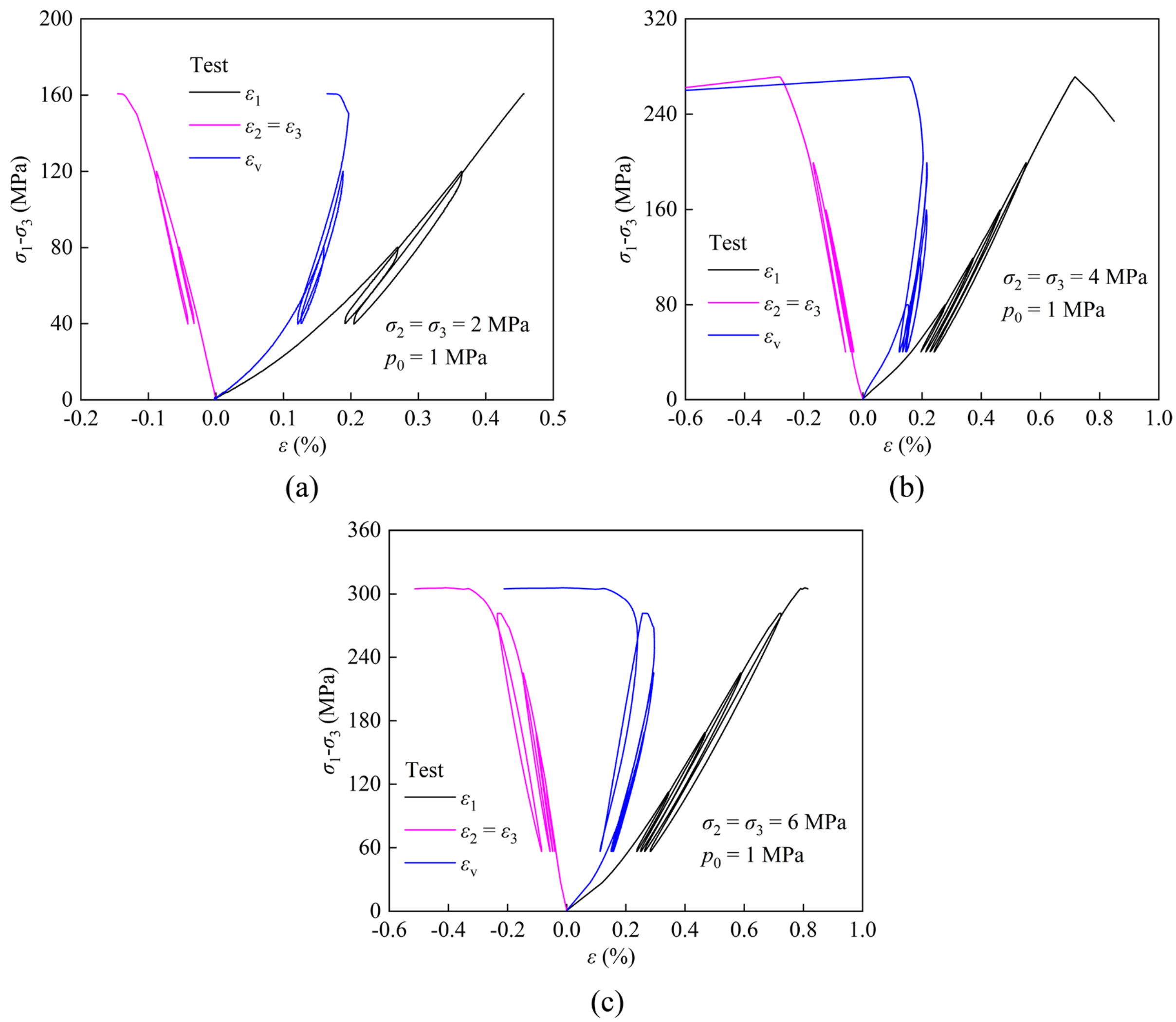

Fig. 4 Stress–strain curves of granite gneiss under triaxial cyclic loading and unloading hydro-mechanical coupling test. **a** $p_0=1$ MPa, $\sigma_3=2$ MPa; **b** $p_0=1$ MPa, $\sigma_3=4$ MPa; **c** $p_0=1$ MPa, $\sigma_3=6$ MPa

coupling tests with confining pressures of 2, 4 and 6 MPa and pore pressures of 1 MPa are shown in Fig. 4. With increasing confining pressure, the peak strength and corresponding deformation of rock increase obviously. In the process of stress loading and unloading, the compacted microcracks inside rock are continuously relaxed during stress unloading, and the deformation and Young's modulus of the rock decreases accordingly. When the stress is reloaded, these relaxed microcracks are recompacted, the deformation and Young's modulus of the rock increase accordingly.

3.2 Mechanical parameters and strength characteristics of granite gneiss under hydro-mechanical coupling conditions

Figure 5 defines the basic mechanical parameters in combination with the typical stress–strain curve of granite gneiss under conventional triaxial hydro-mechanical coupling conditions. Point A represents the crack closure stress $\sigma_{cc,}$ which is the end point of rock compaction stage, and ε_{cc} is its corresponding strain. Point B represents the crack initiation stress σ_{ci}. The stress–strain curve between two points A-B is in the linear elastic stage, and the undamaged Young's modulus E_0 can be derived from the ratio of the axial stress increment $\Delta\sigma_1$ to the strain increment $\Delta\varepsilon_1$ ($E_0 = \Delta\sigma_1/\Delta\varepsilon_1$). Poisson's ratio υ can be derived from the ratio of the lateral strain increment $\Delta\varepsilon_3$ to the axial strain increment $\Delta\varepsilon_1$ ($\upsilon = \Delta\varepsilon_3/\Delta\varepsilon_1$). Point C represents the initial yield strength σ_y of rock, which is the starting point of nonlinear behavior after the linear elastic stage of stress–strain curve, and ε_y is its corresponding to strain. Point D represents the peak strength σ_p of rock, and ε_p is its corresponding strain.

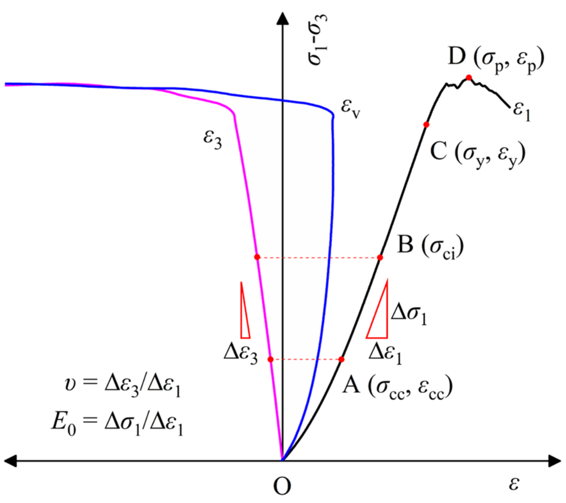

Fig. 5 Definition of mechanical parameters based on typical stress–strain curves of granite gneiss. (E_0 is Young's modulus; υ is Poisson's ratio; σ_{cc} and ε_{cc} are crack closure stress and corresponding to strain; σ_{ci} is crack initiation stress; σ_y and ε_y are initial yield strength and corresponding to strain; σ_p and ε_p are the peak strength and the corresponding to strain)

3.2.1 *Conventional triaxial hydro-mechanical coupling test*

The basic mechanical parameters (E_0, υ, σ_{cc}, ε_{cc}, σ_y, ε_y, σ_p, ε_p) of granite gneiss in conventional triaxial hydro-mechanical coupling test under different confining pressures and pore pressures are listed in Table 1. The mechanical behaviors of rock are closely related to confining pressure and pore pressure. With increasing confining pressure ($\sigma_3 = 2$, 4, 6 MPa) and at same pore pressure ($p_0 = 1$ MPa), the peak strength and initial yield strength of rock increased (Fig. 6a). With increasing pore pressure ($p_0 = 1$, 2, 3 MPa) and at same confining pressure ($\sigma_3 = 4$ MPa), the peak strength and initial yield strength of rock decreased (Fig. 6b). With the change in confining pressure and pore pressure, the undamaged Young's modulus E_0 and Poisson's ratio υ of granite gneiss do not change obviously, and it can be inferred that these two parameters are not dependent on confining pressure and pore pressure.

Table 1 Strength and deformation parameters of granite gneiss under conventional triaxial hydro-mechanical coupling test

σ_3 (MPa)	p_0 (MPa)	E_0 (GPa)	υ	σ_{cc} (MPa)	ε_{cc} (%)	σ_y (MPa)	ε_y (%)	σ_p (MPa)	ε_p (%)
2	1	44.13	0.29	51.23	0.19	192.85	0.53	213.99	0.67
4	1	44.36	0.28	43.81	0.20	231.30	0.64	256.87	0.75
4	2	44.13	0.32	47.63	0.18	216.73	0.55	245.28	0.64
4	3	43.12	0.29	15.71	0.03	211.88	0.62	229.49	0.73
6	1	43.36	0.25	59.97	0.21	262.99	0.69	282.12	0.79

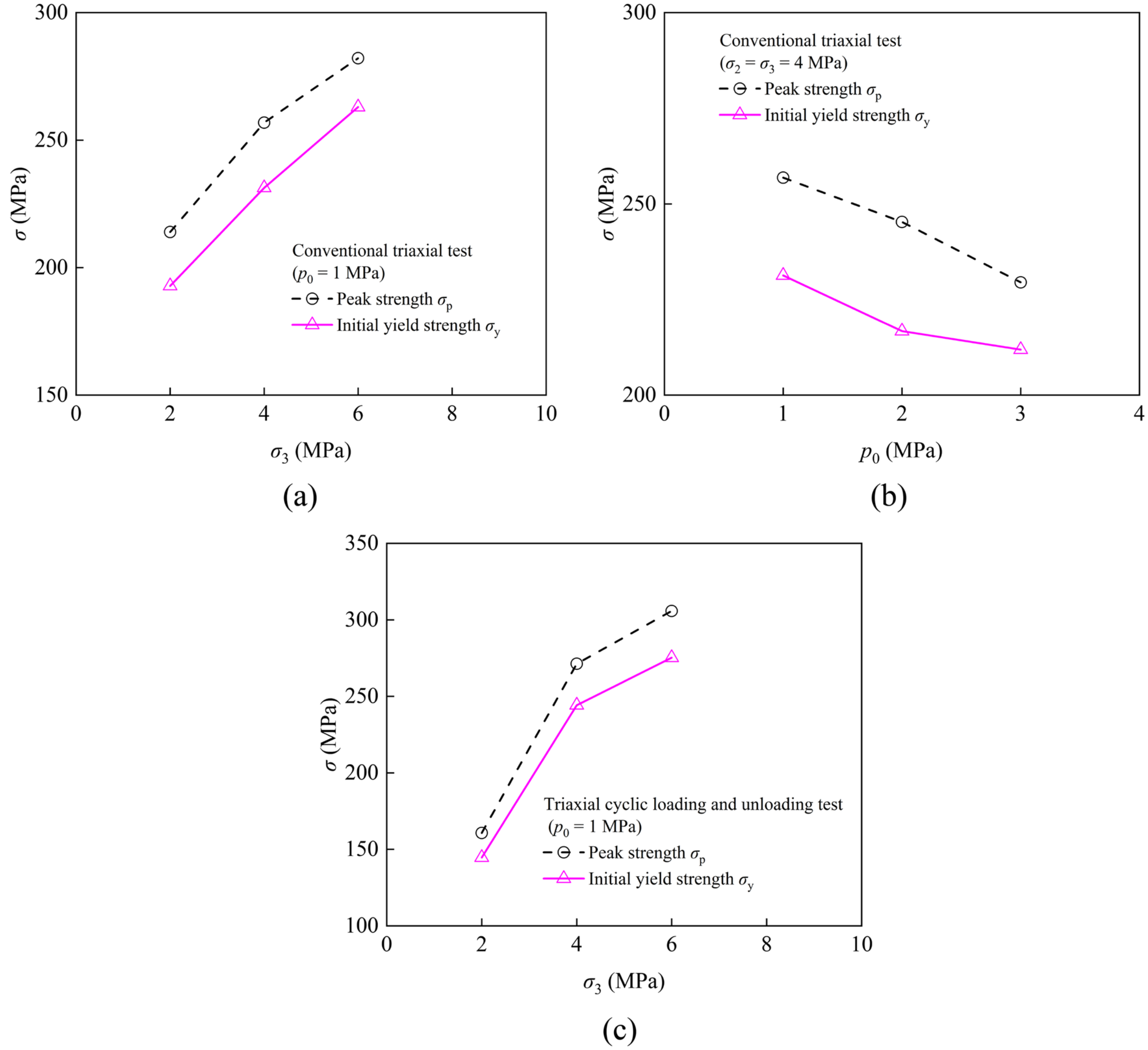

Fig. 6 Variation of the peak strength σ_p and initial yield strength σ_y of granitic gneiss under different σ_3 and p_0. Conventional triaxial hydro-mechanical coupling test: **a** $p_0=1$ MPa, $\sigma_3=2$, 4, 6 MPa; **b** $\sigma_3=4$ MPa, $p_0=1$, 2, 3 MPa; triaxial cyclic loading and unloading hydro-mechanical coupling test: **c** $p_0=1$ MPa, $\sigma_3=2$, 4, 6 MPa

3.2.2 Triaxial cyclic loading and unloading hydro-mechanical coupling test

The basic mechanical parameters (E_0, υ, σ_{cc}, ε_{cc}, σ_y, ε_y, σ_p, ε_p) of granite gneiss under different confining pressures and pore pressures in triaxial cyclic loading and unloading hydro-mechanical coupling tests are listed in Table 2. Similar to the results of conventional triaxial hydro-mechanical coupling test, the peak strength and initial yield strength of rock vary with the confining pressure ($p_0=1$ MPa, $\sigma_3=2$, 4, 6 MPa), as shown in Fig. 6c.

The peak strength of granite gneiss is different under conventional triaxial compression and cyclic loading and unloading hydro-mechanical coupling tests due to different test loading methods, and the strength parameters of these two tests can be fitted separately, as shown in Fig. 7. According to the effective stress principle, there is a linear relationship between the first invariance of effective stress tensor

Table 2 Strength and deformation parameters of granite gneiss under cyclic triaxial loading and unloading hydro-mechanical coupling test

σ_3 (MPa)	p_0 (MPa)	E_0 (GPa)	υ	σ_{cc} (MPa)	ε_{cc} (%)	σ_y (MPa)	ε_y (%)	σ_p (MPa)	ε_p (%)
2	1	43.38	0.23	38.25	0.15	144.63	0.42	160.70	0.46
4	1	44.15	0.30	50.67	0.19	244.2	0.65	271.33	0.72
6	1	45.13	0.26	51.80	0.18	275.27	0.72	305.86	0.80

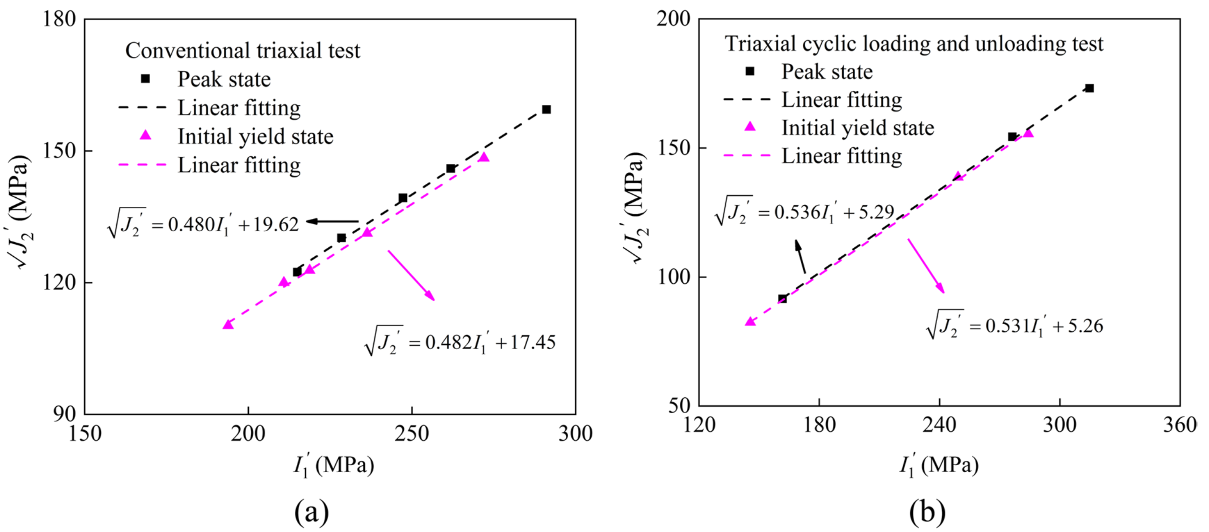

Fig. 7 The effective strength test results and Drucker−Prager linear fitting with the first invariant of effective stress tensor I_1' and the second invariant of effective deviatoric stress $\sqrt{J_2'}$ in peak state and initial yield state. **a** Conventional triaxial hydro-mechanical coupling test result; **b** triaxial cyclic loading and unloading hydro-mechanical coupling test result

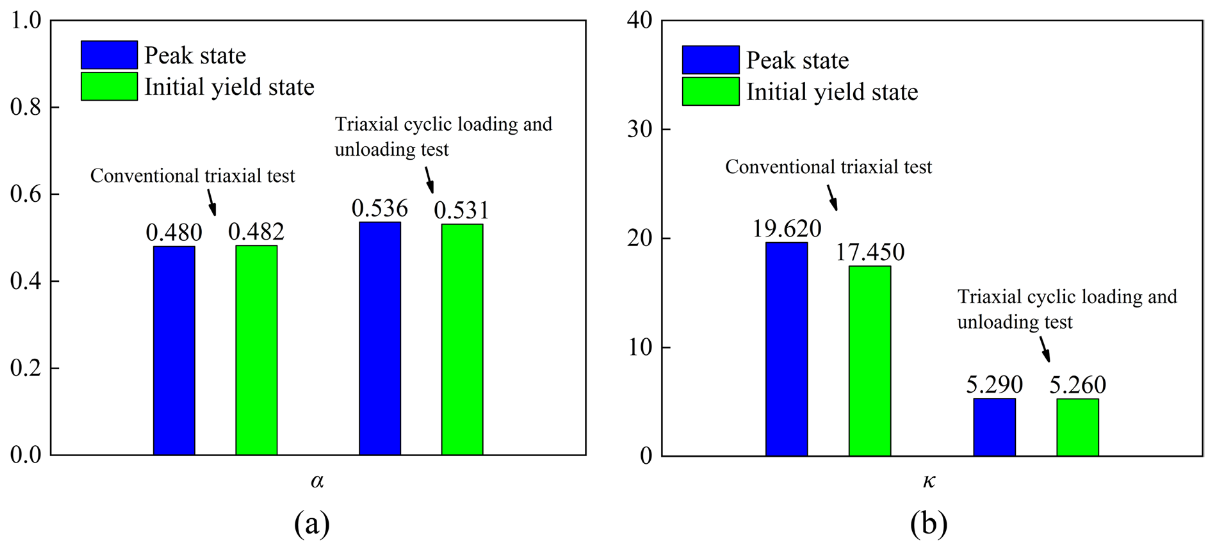

Fig. 8 Strength parameters α and κ under conventional triaxial hydro-mechanical coupling test and triaxial cyclic loading and unloading hydro-mechanical coupling test. **a** Parameter α; **b** parameter κ

I_1' and the second invariance of effective deviatoric stress $\sqrt{J_2'}$ in the peak state and the initial yield state under different confining pressures and pore pressures. The Drucker−Prager criterion can be introduced for linear fitting (Alejano and Bobet 2012):

$$\sqrt{J_2'} = \alpha I_1' + \kappa \tag{1}$$

$$J_2' = \frac{1}{6}\left[(\sigma_1' - \sigma_2')^2 + (\sigma_2' - \sigma_3')^2 + (\sigma_3' - \sigma_1')^2\right]; I_1' = (\sigma_1' + \sigma_2' + \sigma_3') \tag{2}$$

$$\boldsymbol{\sigma}' = \boldsymbol{\sigma} - bp_0\boldsymbol{\delta} \tag{3}$$

where α and κ are the strength parameters; p_0 is the pore pressure; b is the effective stress coefficient, which can be valued as 1 for the rock porous medium material; $\boldsymbol{\delta}$ is a second-order unit tensor; $\boldsymbol{\sigma}$ is the stress tensor; and $\boldsymbol{\sigma}'$ is the effective stress tensor.

Figure 7a shows the strength parameter fitting results of the conventional triaxial hydro-mechanical coupling test, and Fig. 7b shows the strength parameter fitting results of the triaxial cyclic loading and unloading hydro-mechanical coupling test. Finally, the strength parameters of the peak state and the initial yield state of the conventional triaxial hydro-mechanical coupling test are α = 0.480, κ = 19.62 and α = 0.482, κ = 17.45 (see Fig. 8a); the strength parameters of the peak state and initial yield state of the triaxial cyclic loading and unloading hydro-mechanical coupling test are α = 0.536, κ = 5.29 and α = 0.531, κ = 5.26 (see Fig. 8b).

4 A new thermodynamic hydro-mechanical coupling damage constitutive model considering the compaction effect, pre-peak hardening and post-peak softening behaviors

The coupling of plastic deformation and mechanical damage leads to the nonlinear behaviour and failure of rock. Based on the ideal elastic−plastic yield function, a function of the plastic variable and damage variable can be introduced to describe the nonlinear behaviors of rock. The plastic variable can describe the pre-peak plastic hardening behavior of rock, and the damage variable can model the post-peak damage softening behavior of rock (Shao et al. 2006). According to a large number of existing tests, confining pressure and pore pressure are considered to be closely related to the mechanical behaviors of rock (Tenthorey et al. 2003; Zhang et al. 2020). To study the mechanical and deformation characteristics of granite gneiss under hydro-mechanical coupling conditions, a hydro-mechanical coupling damage constitutive model within the framework of irreversible thermodynamics was established.

4.1 Framework of irreversible thermodynamics

The deformation of rock is considered to be divided into two parts: elastic reversible deformation and plastic irreversible deformation. Generally, rock is assumed to be a material with only small deformation. According to the traditional elastic−plastic mechanics theory, the deformation of rock can be expressed as:

$$\boldsymbol{\varepsilon} = \boldsymbol{\varepsilon}^{\mathrm{e}} + \boldsymbol{\varepsilon}^{\mathrm{p}} \text{ and } d\boldsymbol{\varepsilon} = d\boldsymbol{\varepsilon}^{\mathrm{e}} + d\boldsymbol{\varepsilon}^{\mathrm{p}} \tag{4}$$

where $\boldsymbol{\varepsilon}^{\mathrm{e}}$ = elastic strain tensor; $\boldsymbol{\varepsilon}^{\mathrm{p}}$ = plastic strain tensor; and $\boldsymbol{\varepsilon}$ = total strain tensor.

Rock damage occurs with stress loading, and rock damage feeds back to the evolution of rock mechanical properties. Generally, the damage variable of rock can be expressed by the acoustic emission ring count or deterioration of the Young's modulus (Lemaitre 1984; Xue et al. 2022). According to the continuum damage mechanics theory, a scalar damage variable is defined by the deterioration of the Young's modulus during loading:

$$\omega = 1 - \frac{E}{E_0} \tag{5}$$

where E_0 = the undamaged Young's modulus of rock; E = E_0(1-ω) is the damage Young's modulus of rock during loading, which can be obtained through triaxial cyclic loading and unloading tests; and ω is a scalar damage variable with a value range of 0–1.

In the process of irreversible plastic and damage, the thermodynamic potential ψ affected by plastic and damage variables can be divided into two parts:

$$\begin{aligned}\psi(\varepsilon^{\mathrm{e}}, \gamma_p, \omega) &= \psi_e(\varepsilon^e, \omega) + \psi_p(\gamma_p, \omega)\\ &= \frac{1}{2}\boldsymbol{\varepsilon}^e : \mathbf{C}(\omega) : \boldsymbol{\varepsilon}^e + \psi_p(\gamma_p, \omega)\end{aligned} \tag{6}$$

where $\psi_e(\boldsymbol{\varepsilon}^e, \omega)$—the elastic part of the thermodynamic potential; $\psi_p(\gamma_p, \omega)$—the plastic part of the thermodynamic potential; γ_p—the equivalent plastic shear strain; and $\boldsymbol{C}(\omega)$ = the rock damage stiffness matrix, which can be written as:

$$\boldsymbol{C}(\omega) = 2\mu(\omega)(\boldsymbol{I} - \boldsymbol{J}) + 3k(\omega)\boldsymbol{J} \tag{7}$$

where $\mu(\omega)$ = the effective shear modulus; $k(\omega)$ = the effective bulk modulus; $\boldsymbol{I}$ = the fourth-order unit tensor; and $\boldsymbol{J}$ = the fourth-order tensor, which is:

$$\boldsymbol{J} = \frac{1}{3}\boldsymbol{\delta} \otimes \boldsymbol{\delta} \tag{8}$$

where $\boldsymbol{\delta}$ = the second-order unit tensor; and the symbol '$\otimes$' indicates the Kronecker product.

Since it is difficult to obtain an accurate expression for the thermodynamic potential plastic part, according to the existing research results (Chen et al. 2015; Jia et al. 2021), the expression for the thermodynamic potential plastic part can be introduced as:

$$\psi_p(\gamma_p, \omega) = \zeta(1-\omega)\left[h_1\gamma_p - \left(h_1 - h_0\right)\eta \ln \frac{\eta + \gamma_p}{\eta}\right] \tag{9}$$

where parameters h_0, h_1, ζ and η control the plastic part characteristics of the thermodynamic potential.

According to the second law of thermodynamics, the Clausius−Duhem dissipation inequality is:

$$\boldsymbol{\sigma} : d\boldsymbol{\varepsilon}^\mathrm{p} - d\psi \geq 0 \tag{10}$$

where the sign ':' = the second-order dot production.

The thermodynamic forces Y_e, Y_p, Y_d can be derived by differentiating the thermodynamic potential:

$$Y_\mathrm{e} = -\frac{\partial \psi_e}{\partial \omega} \tag{11}$$

$$Y_\mathrm{p} = -\frac{\partial \psi_p}{\partial \gamma^p} \tag{12}$$

$$Y_\mathrm{d} = -\frac{\partial \psi_p}{\partial \omega} \tag{13}$$

To satisfy Eq. (10), the following equation can be derived:

$$\boldsymbol{\sigma} = \frac{\partial \psi}{\partial \boldsymbol{\varepsilon}^e} = \boldsymbol{C}(\omega) : (\boldsymbol{\varepsilon} - \boldsymbol{\varepsilon}^p) \tag{14}$$

The differential form of Eq. (14) can be written as:

$$d\boldsymbol{\sigma} = \boldsymbol{C}(\omega) : (d\boldsymbol{\varepsilon} - d\boldsymbol{\varepsilon}^p) - \boldsymbol{C}_0 : (\boldsymbol{\varepsilon} - \boldsymbol{\varepsilon}^p)d\omega \tag{15}$$

where $\boldsymbol{C}_0$ = the initial elastic stiffness matrix.

4.2 Elastoplastic hydro-mechanical coupling damage constitutive relationship

According to the strength results of granite gneiss in Sect. 3.2, the Drucker−Prager yield function can better meet the strength characteristics of granite gneiss. Therefore, according to the effective stress principle, a function that can describe the nonlinear behavior of rock can be introduced on the basis of the Drucker−Prager yield criterion to better model the deformation characteristics of rock:

$$f_p = \alpha I_1' + \sqrt{J_2'} - \frac{\kappa h}{\zeta} \leq 0 \tag{16}$$

where h is a function controlling the hardening and softening characteristics of rock. There are four parameters (ζ, h_1, h_0, η) in the function h, which can be derived from the thermodynamic force Y_p:

$$h(\gamma_p, \omega) = \frac{\partial \psi_p}{\partial \gamma_p} = -Y_\mathrm{p} = \zeta(1-\omega)\left[h_1 + \left(h_1 - h_0\right)\frac{\gamma_p}{\eta + \gamma_p}\right] \tag{17}$$

$$d\gamma_p = \sqrt{\frac{2}{3}d\mathbf{e}^p : d\mathbf{e}^p}, d\mathbf{e}^p = d\boldsymbol{\varepsilon}^p - \frac{1}{3}tr(d\boldsymbol{\varepsilon}^p)\boldsymbol{\delta} \tag{18}$$

where $\boldsymbol{e}^\mathrm{p}$ = the plastic partial strain tensor; parameter η controls the characteristic rate of plastic hardening of rock; parameter h_0 controls the characteristics of the initial yield surface; and parameter h_1 controls the characteristics of the plastic failure surface.

Rock shows different pre-peak nonlinear behavior under different effective stress (Wang et al. 2020). An exponential function between the control hardening characteristic parameter η and the effective stress can be proposed:

$$\eta(\sigma_3') = a_1 e^{a_2\sigma_3'} + a_3 \tag{19}$$

where parameters a_1, a_2, and a_3 control the characteristics of η.

The non-associated plastic potential function can be expressed as:

$$g = \alpha_g I_1' + \sqrt{J_2'} \le 0 \tag{20}$$

where $\alpha_{\mathrm{g}} = \alpha$.

According to Hooke's law, the effective stress increment can be expressed as:

$$d\boldsymbol{\sigma}' = \boldsymbol{C}(\omega) : (d\boldsymbol{\varepsilon} - d\boldsymbol{\varepsilon}^p) \tag{21}$$

where the plastic strain increment $d\boldsymbol{\varepsilon}_{\mathrm{p}}$ can be determined according to the plastic flow law:

$$d\boldsymbol{\varepsilon}^p = d\lambda_p \frac{\partial g}{\partial \boldsymbol{\sigma}'} \tag{22}$$

where $d\lambda_{\mathrm{p}}$ = the plastic multiplier, which is non-negative, and $\partial g / \partial \boldsymbol{\sigma}'$ determines the direction of plastic flow.

According to the traditional plastic mechanics theory, the loading and unloading are given by the Kuhn–Tucker condition:

$$d\lambda_p \ge 0; \quad f_p(\boldsymbol{\sigma}', \gamma_p, \omega) \le 0; d\lambda_p f_p(\boldsymbol{\sigma}', \gamma_p, \omega) = 0 \tag{23}$$

In the plastic deformation and damage process of rock, the stress falls on the yield surface and satisfies the plastic consistency condition $df_{\mathrm{p}} = 0$:

$$df_p(\boldsymbol{\sigma}', \gamma_p) = \frac{\partial f_p}{\partial \sqrt{J_2'}} \frac{\partial \sqrt{J_2'}}{\partial \boldsymbol{\sigma}'} d\boldsymbol{\sigma}' + \frac{\partial f_p}{\partial I_1'} \frac{\partial I_1'}{\partial \boldsymbol{\sigma}'} d\boldsymbol{\sigma}' + \frac{\partial f_p}{\partial \gamma_p} d\gamma_p = 0 \tag{24}$$

The new expression of the effective stress increment tensor is obtained by substituting Eq. (22) into Eq. (21):

$$d\boldsymbol{\sigma}' = \boldsymbol{C}(\omega) : (d\boldsymbol{\varepsilon} - d\lambda_p \frac{\partial g}{\partial \boldsymbol{\sigma}'}) \tag{25}$$

Then substituting the effective stress increment tensor (Eq. (25)) into the plastic consistency condition (Eq. (24)), the following can be obtained:

$$df_p(\boldsymbol{\sigma}', \gamma_p) = \frac{\partial f_p}{\partial \boldsymbol{\sigma}'} : \boldsymbol{C}(\omega) : (d\boldsymbol{\varepsilon} - d\lambda_p \frac{\partial g}{\partial \boldsymbol{\sigma}'}) + \frac{\partial f_p}{\partial \gamma_p} \frac{\partial \gamma_p}{\partial \boldsymbol{\varepsilon}^p} \frac{\partial g}{\partial \boldsymbol{\sigma}'} d\lambda_p = 0 \tag{26}$$

Finally, the expression of the plastic multiplier can be derived:

$$d\lambda_p = \frac{\frac{\partial f_p}{\partial \boldsymbol{\sigma}'} : \boldsymbol{C}(\omega) : d\boldsymbol{\varepsilon}}{H(\gamma_p, \omega)} \tag{27}$$

$$H(\gamma_p, \omega) = \frac{\partial f_p}{\partial \boldsymbol{\sigma}'} : \boldsymbol{C}(\omega) : \frac{\partial g}{\partial \boldsymbol{\sigma}'} - \frac{\partial f_p}{\partial \gamma_p} \frac{\partial \gamma_p}{\partial \boldsymbol{\varepsilon}^p} \frac{\partial g}{\partial \boldsymbol{\sigma}'} \tag{28}$$

In addition, the stress–strain relationship of rock (Eq. (21)) can be simplified as:

$$d\boldsymbol{\sigma}' = \boldsymbol{C}^{ep}(\gamma_p, \omega) : d\boldsymbol{\varepsilon} \tag{29}$$

where $\boldsymbol{C}^{\mathrm{ep}}$ = the elastic−plastic tangent stiffness matrix of rock, which can be derived by substituting Eq. (27) into Eq. (21):

$$\boldsymbol{C}^{ep}(\gamma_p, \omega) = \boldsymbol{C}(\omega) - \frac{\boldsymbol{C}(\omega) : \frac{\partial f_p}{\partial \sigma'} : \frac{\partial g}{\partial \sigma'} : \boldsymbol{C}(\omega)}{H(\gamma_p, \omega)} \tag{30}$$

4.3 Irreversible damage evolution for rock nonlinear softening behavior

Irreversible damage of rock leads to nonlinear softening behavior. Generally, irreversible damage is described by the damage variable, which can be updated according to the damage evolution function and driven by the damage force (Shao et al. 2006; Jia et al. 2021). The following exponential damage evolution function was introduced:

$$f_{\mathrm{d}}\left(Y_{\mathrm{d}}, \omega\right) = \omega_{\mathrm{c}}[1 - \exp(-B_{\omega} Y_{\mathrm{d}})] - \omega \le 0 \tag{31}$$

$$Y_{\mathrm{d}}(\gamma_p) = -\frac{\partial \psi_p}{\partial \omega} = \zeta \left[h_1 \gamma_p - \left(h_1 - h_0\right) \eta \ln \frac{\eta + \gamma_p}{\eta} \right] \tag{32}$$

where ζ controls softening characteristic; B_{ω} controls the damage rate, ω_{c} controls the damage threshold, and the damage force Y_{d} is derived from the plastic part of the thermodynamic potential.

Similar to plasticity, the damage variable needs to meet the consistency condition ($df_{\mathrm{d}} = 0$). The differential of Eq. (31) can be written as:

$$df_{\mathrm{d}} = \frac{\partial f_{\mathrm{d}}}{\partial Y_{\mathrm{d}}} dY_{\mathrm{d}} + \frac{\partial f_{\mathrm{d}}}{\partial \omega} d\omega = 0 \tag{33}$$

$$d\omega = \frac{\partial f_{\mathrm{d}}}{\partial Y_{\mathrm{d}}} dY_{\mathrm{d}} \tag{34}$$

Rock shows different post-peak nonlinear behaviors under different effective stress (Shi et al. 2017). An exponential function between the control softening characteristic parameter ζ and the effective stresses was provided:

$$\zeta(\sigma_3') = b_1 e^{b_2 \sigma_3'} + b_3 \tag{35}$$

where parameters b_1, b_2, and b_3 control the characteristics of ζ.

4.4 Characterization of the initial compaction effect of rock

There are inevitably a large number of initial micropores and microcracks inside rock. During the loading process of the compression test, the rock undergoes the compaction stage (Baud et al. 2000; Cai et al. 2004; Zhu et al. 2022), and the micropores and microcracks gradually close under the pressure. In this stage, the rock stiffness increases continuously and finally tends to be stable. This phenomenon is shown as a concave curve with an increasing undamaged Young's modulus on the pre-peak stress–strain curve, as shown in Fig. 9. If the undamaged Young's modulus of rock is set to a fixed value, the characteristics of the pre-peak compaction stage of rock cannot be well expressed. Therefore, a compaction function C_{k} can be introduced to characterize the change in Young's modulus in the compaction stage:

$$E = C_{\mathrm{k}}(1-\omega)E_0 \tag{36}$$

$$C_{\mathrm{k}} = \begin{cases} \log_m \left[\frac{(m-1)\varepsilon_1}{\varepsilon_{\mathrm{cc}}} + 1\right] & \varepsilon_1 < \varepsilon_{\mathrm{cc}} \\ 1 & \varepsilon_1 \geq \varepsilon_{\mathrm{cc}} \end{cases} \tag{37}$$

where m is a constant that can be obtained according to the compaction stage of rock.

In the initial loading process of rock, the initial micropores and microcracks in rock begin to be compacted, and rock enters the compaction stage. As shown in Fig. 9, in the compaction stage of rock,

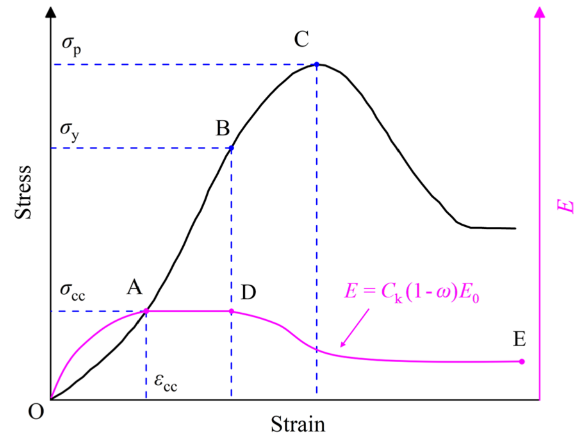

Fig. 9 The evolution Young's modulus E of rock in the whole failure process. (OA is the compaction stage, AB is the linear elastic stage, BC is the hardening stage, OA represents the undamaged Young's modulus increases under the influence of compaction effect, AD represents undamaged Young's modulus E_0 tends to be stable, DE represents deterioration of Young's modulus due to damage)

the increase in the undamaged Young's modulus of rock can be characterized by the proposed compaction function. As micropores and microcracks continue to compress and tend to close, rock enters the linear elastic stage. In this stage, the undamaged Young's modulus of rock tends to be stable, and the value of the compaction function tends to 1. As the stress continues to load, new cracks occur inside rock, resulting in the continuous deterioration and damage of rock. At this time, the value of the compaction function is constant at 1, and the damage variable begins to increase, resulting in the continuous deterioration of the Young's modulus of rock.

4.5 Numerical realization of the proposed model

4.5.1 Secondary development of the proposed model in finite element program

The proposed model cannot be directly used in ABAQUS software, so it is necessary to carry out secondary development of ABAQUS and prepare a user-defined material subroutine (UMAT). The UMAT subroutine is compiled in the FORTRAN language: (1) first, calculate the elastic predicted effective stress $\boldsymbol{\sigma}'^{,\mathrm{trial}}$, and calculate $\eta(\sigma_3')$ and $\zeta(\sigma_3')$; (2) according to the predicted stress, calculate whether the yield function $f_{\mathrm{p}}^{\mathrm{trial}}$ is greater than zero. If the yield function is less than f_{t} ($f_{\mathrm{t}}=1\times10^{-8}$), elastic prediction is effective, the stress, strain and other variables are updated, and the program is terminated; (3) if the yield function is greater than f_{t}, it means that the stress state has exceeded the yield surface, and the stress needs to be corrected; (4) update relevant variables and check whether the consistency conditions are met. If not, return to step 2.

4.5.2 Cutting plane return mapping integral method

To verify the correctness of the proposed model, the finite element program of the proposed model can be established in combination with the finite element software ABAQUS. And the return mapping integral method is an effective method to realize the proposed model. In this work, the finite element program of the proposed model can be compiled in the cutting plane return mapping integral method (Simo and Taylor 1986; Xu and Prévost 2016). The cutting plane return mapping integral method mainly includes two parts: elastic prediction and stress correction. The geometric interpretation of the cutting plane return mapping integral method is shown in Fig. 10. The Taylor expansion of the yield function of the $k+1$th step can be written as:

$$f_{\mathrm{p},n}^{k+1}=f_{\mathrm{p},n-1}^{k+1}+\frac{\partial f_{\mathrm{p},n-1}^{k+1}}{\partial\boldsymbol{\sigma}'}:\Delta\boldsymbol{\sigma}'+\frac{\partial f_{\mathrm{p},n-1}^{k+1}}{\partial\gamma_{\mathrm{p}}}\Delta\gamma_{\mathrm{p}}\approx0 \tag{38}$$

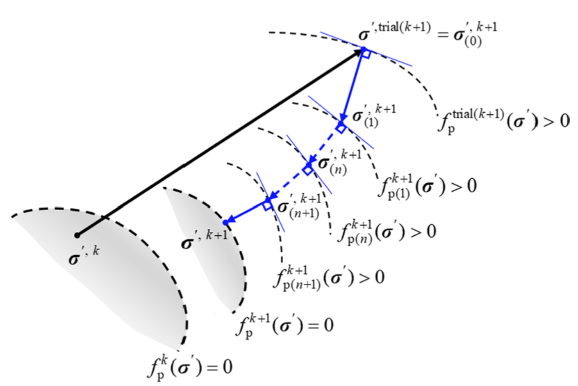

Fig. 10 Geometric interpretation of cutting plane return mapping integral method (Simo and Taylor 1986; Xu and Prévost 2016)

Input: $\boldsymbol{\sigma}'^{,k}$, $\boldsymbol{\varepsilon}^{k}$, $\boldsymbol{\varepsilon}^{\mathrm{e}(k)}$, $\boldsymbol{\varepsilon}^{\mathrm{p}(k)}$, γ_{p}^{k}, ω^{k}

Read: E_0, υ, α, κ, h_1, h_0, η, ζ, ω, ω_{c}, B_{ω}, m

Calculate: C_{k}, $\boldsymbol{C}(\omega^{k})$

For $k=0$, …, sum

Elastic prediction

$\boldsymbol{\varepsilon}^{k+1}=\boldsymbol{\varepsilon}^{k}+d\boldsymbol{\varepsilon}^{k+1}$

$\boldsymbol{\varepsilon}^{\mathrm{p}(k+1)}=\boldsymbol{\varepsilon}^{\mathrm{p}(k)}$

$\boldsymbol{\varepsilon}^{\mathrm{e}(k+1)}=\boldsymbol{\varepsilon}^{\mathrm{e}(k)}+d\boldsymbol{\varepsilon}^{k+1}$

$\boldsymbol{\sigma}'^{,k+1}=\boldsymbol{\sigma}'^{,k}+C_{\mathrm{k}}\boldsymbol{C}(\omega^{k})d\boldsymbol{\varepsilon}^{k+1}$

$\gamma_{\mathrm{p}}^{k+1}=\gamma_{\mathrm{p}}^{k}$

$\omega^{k+1}=\omega^{k}$

Calculate: $\eta(\sigma_3')$ and $\zeta(\sigma_3')$

DO WHILE $f_{\mathrm{p}}\left(\boldsymbol{\sigma}'^{,k+1},\ \gamma_{\mathrm{p}}^{k+1},\ \omega^{k+1}\right)\geq f_{\mathrm{t}}$ (Stress correction)

Calculate: $\Delta^2\lambda_{\mathrm{p}}^{k+1}$

$d\boldsymbol{\varepsilon}^{\mathrm{p}(k+1)}=\Delta^2\lambda_{\mathrm{p}}^{k+1}\dfrac{\partial g}{\partial\boldsymbol{\sigma}'}$

$d\gamma_{\mathrm{p}}^{k+1}=\Delta^2\lambda_{\mathrm{p}}^{k+1}\dfrac{\partial g}{\partial\sqrt{J_2'}}$

$d\omega^{k+1}=\dfrac{\partial f_{\mathrm{d}}}{\partial Y_d}dY_d^{k+1}$

$\Delta\lambda_{\mathrm{p}}^{k+1}=\Delta\lambda_{\mathrm{p}}^{k+1}+\Delta^2\lambda_{\mathrm{p}}^{k+1}$

$\omega^{k+1}=\omega^{k+1}+d\omega^{k+1}$

$\gamma_{\mathrm{p}}^{k+1}=\gamma_{\mathrm{p}}^{k+1}+d\gamma_{\mathrm{p}}^{k+1}$

$d\boldsymbol{\sigma}'^{,k+1}=C_{\mathrm{k}}\boldsymbol{C}(\omega^{k+1})d\boldsymbol{\varepsilon}^{\mathrm{p}(k+1)}+d\omega^{k+1}C_{\mathrm{k}}\boldsymbol{C}_0\boldsymbol{\varepsilon}^{\mathrm{e}(k+1)}$

$\boldsymbol{\sigma}'^{,k+1}=\boldsymbol{\sigma}'^{,k+1}-d\boldsymbol{\sigma}'^{,k+1}$

$\boldsymbol{\varepsilon}^{\mathrm{p}(k+1)}=\boldsymbol{\varepsilon}^{\mathrm{p}(k+1)}+C_{\mathrm{k}}\boldsymbol{C}^{-1}(\omega^{k+1})d\boldsymbol{\sigma}'^{,k+1}$

$\boldsymbol{\varepsilon}^{\mathrm{e}(k+1)}=\boldsymbol{\varepsilon}^{\mathrm{e}(k)}-C_{\mathrm{k}}\boldsymbol{C}^{-1}(\omega^{k+1})d\boldsymbol{\sigma}'^{,k+1}$

$\boldsymbol{\varepsilon}^{k+1}=\boldsymbol{\varepsilon}^{\mathrm{e}(k+1)}+\boldsymbol{\varepsilon}^{\mathrm{p}(k+1)}$

Update: C_{k}, $\boldsymbol{C}(\omega^{k})$

END DO

Output: $\boldsymbol{\sigma}'^{,k+1}$, $\boldsymbol{\varepsilon}^{k+1}$, $\boldsymbol{\varepsilon}^{\mathrm{e}(k+1)}$, $\boldsymbol{\varepsilon}^{\mathrm{p}(k+1)}$, $\gamma_{\mathrm{p}}^{k+1}$, ω^{k+1}

Fig. 11 user-defined material subroutine (UMAT) algorithm flow with the proposed model

$$\Delta\boldsymbol{\sigma}' = -\Delta^2\lambda_{\mathrm{p},n-1}^{k+1}\boldsymbol{C}_{n-1}^{k+1} : \frac{\partial g_{n-1}^{k+1}}{\partial\boldsymbol{\sigma}'} \tag{39}$$

$$\Delta\gamma_{\mathrm{p},n-1}^{k+1} = \Delta^2\lambda_{\mathrm{p},n-1}^{k+1}\frac{\partial g_{n-1}^{k+1}}{\partial\sqrt{3J'_{2_{n-1}}}^{k+1}} \tag{40}$$

where $\Delta\boldsymbol{\sigma}'$ and $\Delta\gamma_{\mathrm{p}}$ are small increments of effective stress tensor and equivalent plastic shear strain between two steps

Simultaneous Eqs. (38), (39), and (40) can obtain the increment of plastic multiplier $\Delta^2\lambda$:

$$\Delta^2\lambda_{\mathrm{p},n-1}^{k+1} = \frac{f_{\mathrm{p},n-1}^{k+1}}{\frac{\partial f_{p,n-1}^{k+1}}{\partial\boldsymbol{\sigma}'} : \boldsymbol{C}_{n-1}^{k+1} : \frac{\partial g_{n-1}^{k+1}}{\partial\boldsymbol{\sigma}'} - \frac{\partial f_{\mathrm{p},n-1}^{k+1}}{\partial\gamma_{\mathrm{p}}}\frac{\partial g_{n-1}^{k+1}}{\partial\sqrt{J'_{2_{n-1}}}^{k+1}}} \tag{41}$$

$$\Delta\lambda_{\mathrm{p}}^{k+1} = \Delta\lambda_{\mathrm{p}}^{k} + \Delta^2\lambda_{\mathrm{p}}^{k} \tag{42}$$

And the specific UMAT subroutine algorithm flow is shown in Fig. 11.

5 Determination of model parameters and model verification

5.1 Numerical calculation model and boundary condition

A series of numerical simulations were carried out based on the ABAQUS secondary development user-defined material subroutine (UMAT), and the correctness of the proposed model was verified by comparing the numerical simulation results with the test results. As shown in Fig. 12, according to the actual size (diameter: 50 mm, height: 100 mm) of the cylindrical specimen, a numerical calculation model is established, and the model is divided into 10,395 units. The Z coordinate axis in the software is regarded as the σ_1 direction, and the X and Y coordinate axes are

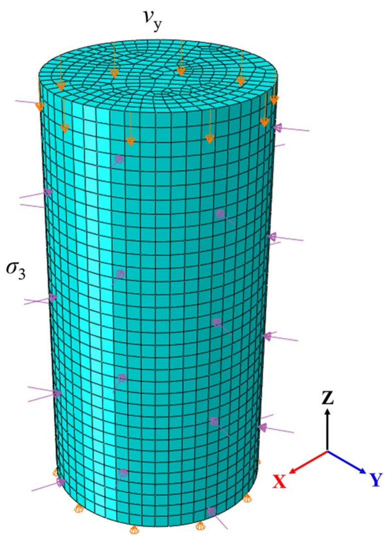

Fig. 12 Element division and boundary conditions of finite element numerical calculation model (Apply vertical restraint at the bottom of the model, apply σ_3 around the model, and apply displacement loading rate (ν_y) on the top of the model)

regarded as the σ_2 and σ_3 directions. Apply a displacement boundary condition on the bottom of the model to constrain the vertical displacement of the model and apply a stress boundary condition around the model with a rate of 0.75 MPa/step to simulate the confining pressure σ_3. A displacement boundary condition is applied on the top surface of the model to simulate the loading process with a rate of ν_y (0.01 mm/step). When applying boundary conditions, confining pressure is first applied to the specified value, and then displacement is applied to the top surface of the model.

5.2 Determination of mechanical parameters and model parameters

Most of the parameters of the proposed model can be determined by laboratory tests. The values of the undamaged Young's modulus E_0, Poisson's ratio υ, and strength parameters α and κ were discussed in

Table 3 Mechanical and model parameters of granitic gneiss under conventional triaxial hydro-mechanical coupling test

σ_3 (MPa)	p_0 (MPa)	E_0 (GPa)	υ	α	κ	h_1	h_0	ω_c	η	ζ	m
2	1										12
4	1										5
4	2	43.82	0.286	0.480	19.62	1.15	0.88	0.5	0.0005	30	6
4	3										14
6	1										6

Table 4 Mechanical and model parameters of granitic gneiss under triaxial cyclic loading and unloading hydro-mechanical coupling test

σ_3 (MPa)	p_0 (MPa)	E_0 (GPa)	υ	α	κ	h_1	h_0	ω_c	η	ζ	m
2	1										14
4	1	44.21	0.263	0.536	5.29	1.20	0.90	0.5	0.0002	30	10
6	1										10

Sect. 3.2. The change in the undamaged Young's modulus E_0 and Poisson's ratio υ under different confining pressures is not obvious, and their average value can be taken. Parameter h_1 controls the position of the plastic failure surface of rock and can be calibrated by numerical simulation tests. Parameter h_0 is the ratio of the initial yield strength to the peak strength. Parameter ω_c can be determined at the final failure stage, which controls the maximum value of the damage variable. Parameters η and ζ can be determined through a series of numerical simulation tests and parameter sensitivity analysis in Sect. 5.3 below. Parameter m of the compaction coefficient is determined by the change characteristics of the undamaged Young's modulus in the compaction stage of the test. Table 3 gives the mechanical and model parameters of granite gneiss under conventional triaxial hydro-mechanical coupling tests; Table 4 gives the mechanical and model parameters of granite gneiss under the triaxial cyclic loading and unloading hydro-mechanical coupling tests.

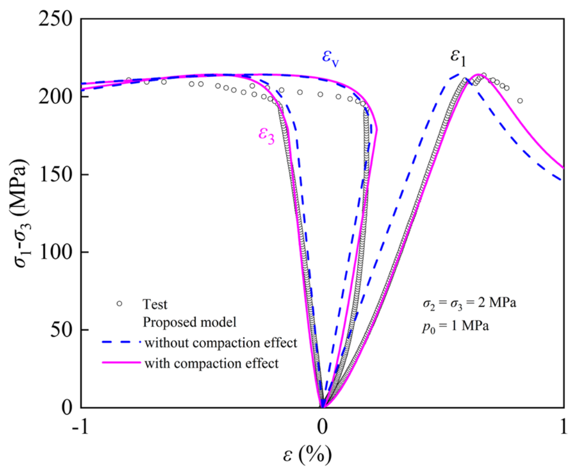

Fig. 14 Comparison of numerical simulation results of the proposed model with and without compaction effect

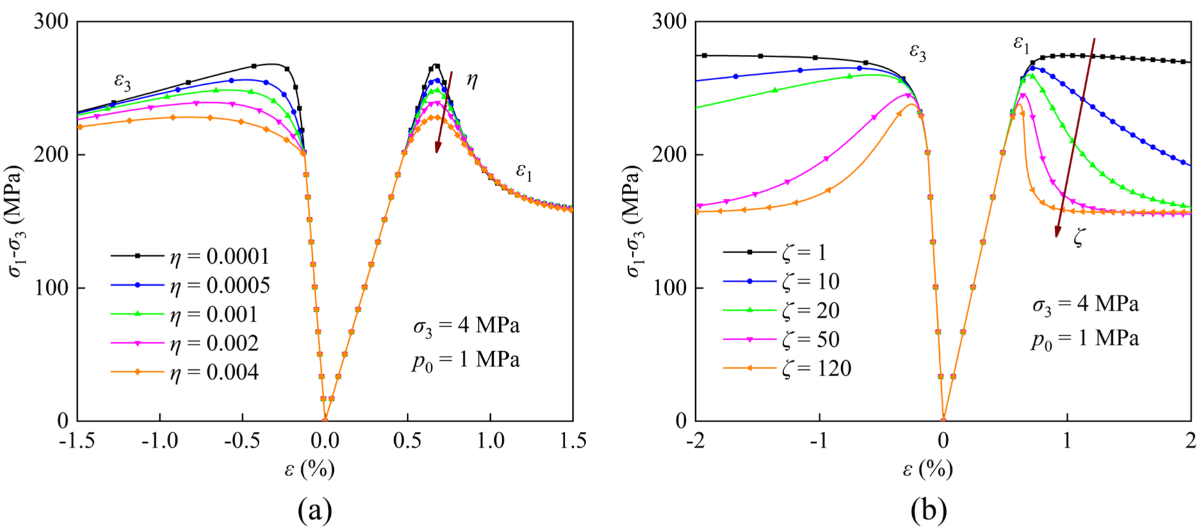

Fig. 13 Sensitivity analysis of the proposed model parameters **a** η and **b** ζ

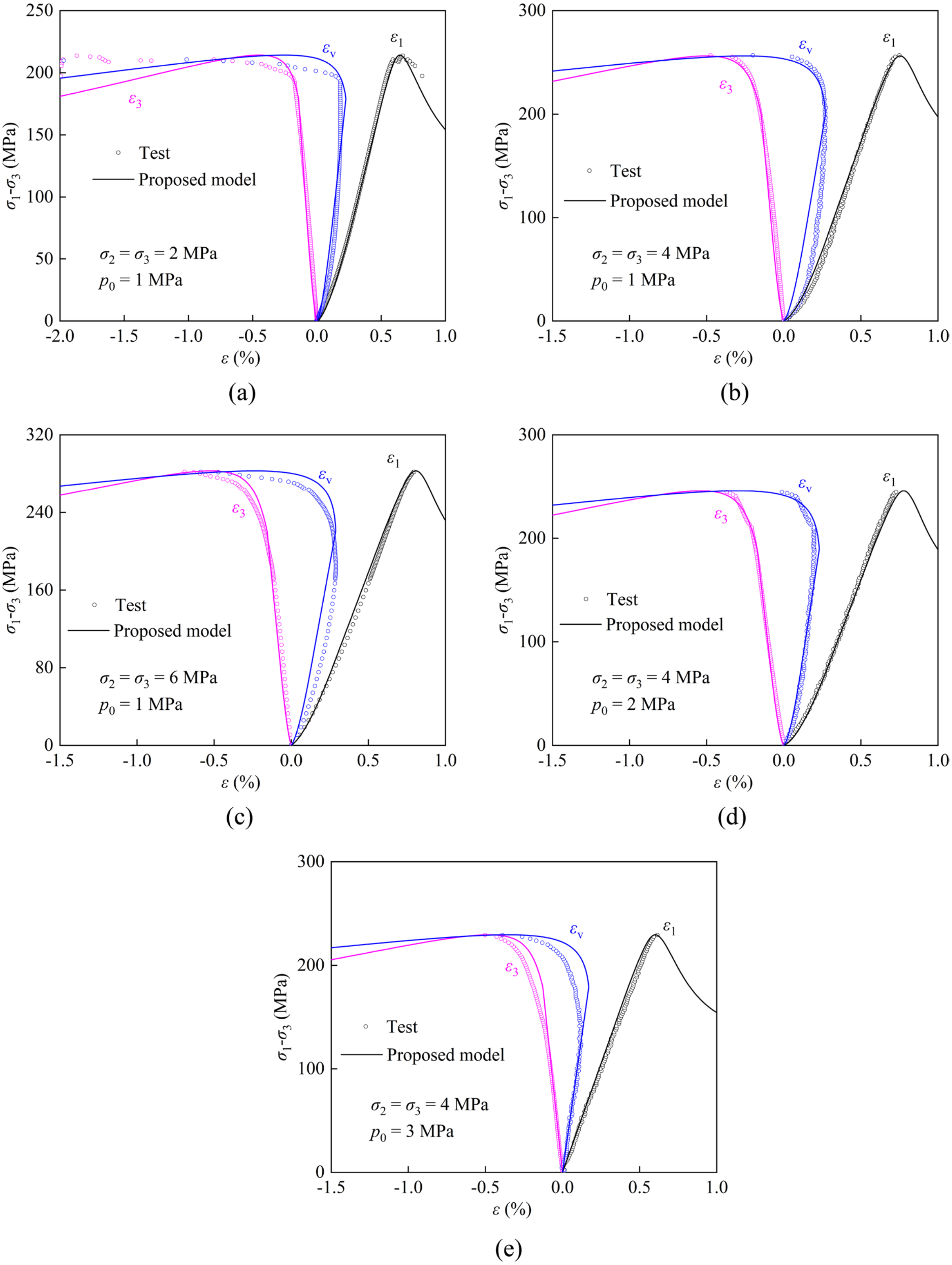

σ_1-σ_3 (MPa)
ε (%)
ε_1
ε_3
ε_v
Test
Proposed model
$\sigma_2 = \sigma_3 = 2$ MPa
$p_0 = 1$ MPa
(a)
$\sigma_2 = \sigma_3 = 4$ MPa
$p_0 = 1$ MPa
(b)
$\sigma_2 = \sigma_3 = 6$ MPa
$p_0 = 1$ MPa
(c)
$\sigma_2 = \sigma_3 = 4$ MPa
$p_0 = 2$ MPa
(d)
$\sigma_2 = \sigma_3 = 4$ MPa
$p_0 = 3$ MPa
(e)

Fig. 15 Comparison of granitic gneiss stress–strain curves between the proposed model simulation results and conventional triaxial hydro-mechanical test results under different σ_3 and p_0. **a** $p_0=1$ MPa, $\sigma_3=2$ MPa; **b** $p_0=1$ MPa, $\sigma_3=4$ MPa; **c** $p_0=1$ MPa, $\sigma_3=6$ MPa; **d** $p_0=2$ MPa, $\sigma_3=4$ MPa; **e** $p_0=3$ MPa, $\sigma_3=4$ MPa

5.3 Sensitivity analysis of the proposed model parameters η and ζ for rock nonlinear behavior

Parameters η and ζ are difficult to obtain directly from the test data. They can achieve the ideal simulation effect through a series of numerical simulation tests. η controls the pre-peak hardening nonlinear behavior of rock, and ζ controls the post-peak softening nonlinear behavior of rock. To study the influence of these two parameters on the simulation results, sensitivity analysis was carried out under the stress conditions of a confining pressure of 4 MPa and a pore pressure of 1 MPa. Other parameters are unchanged and change η (=0.0001, 0.0005, 0.001, 0.002, 0.004), and the sensitivity analysis result is shown in Fig. 13a. And other parameters are unchanged and change ζ (=1, 10, 20, 50, 100, 130), the sensitivity analysis result is shown in Fig. 13b. The more obvious the pre-peak hardening nonlinear behavior of rock with the increase in parameter η; the faster the post-peak softening rate of rock and the more obvious the stress drop with the increase in parameter ζ.

5.4 Comparison of the proposed model simulation results with and without the initial compaction effect

Based on the conventional triaxial stress level ($\sigma_3=2$ MPa and $p_0=1$ MPa), the model numerical simulation result of the stress–strain curve with and without the compaction effect is shown in Fig. 14. The stress–strain curve of the numerical simulation without considering the compaction stage is a straight line in the pre-peak compaction stage. The strain value of the test is slightly larger than the strain value of the numerical simulation under the same stress, and this difference exists in the whole simulation process. The numerical simulation stress–strain curve considering the compaction stage is consistent with the test results in the pre-peak compaction stage, which is a concave curve, and the test and model numerical simulation results are highly consistent. Therefore, it is necessary to introduce the compaction function.

5.5 The proposed model numerical validation with test results

The parameters in Tables 1, 2, 3 and 4 were used to simulate the test results of granite gneiss under different confining pressures and pore pressures. Figure 15 compares the stress–strain curves of granite gneiss under different confining pressures and pore pressures in the conventional triaxial hydro-mechanical coupling test; Fig. 16 compares the stress–strain curves of granite gneiss under different confining pressures and pore pressures in the triaxial cyclic loading and unloading hydro-mechanical coupling test. According to the numerical simulation results, the peak strength of rock increase with increasing confining pressure or decreasing pore pressure, and the change trend is the same as the test results. The results of the proposed model numerical simulation and test are in good agreement. The peak strengths of the proposed model numerical simulation and test under different stress levels are given in Tables 5 and 6. Figure 17 compares the peak strengths of the proposed model numerical simulation and test under different stress levels, and these two have good consistency. The proposed model numerical simulation results show that the strength change trend is the same as the test results. The comparison of the numerical simulation and test proves the correctness and effectiveness of the proposed model.

6 The prediction of the untested stress level with the proposed model

According to the above work, the proposed model can better simulate the mechanical behaviors of granite gneiss under different confining pressures and pore pressures. Therefore, the conventional triaxial hydro-mechanical coupling test of granite gneiss under untested stress levels should be preliminarily predicted. The predicted stress levels can be taken as follows: (1)

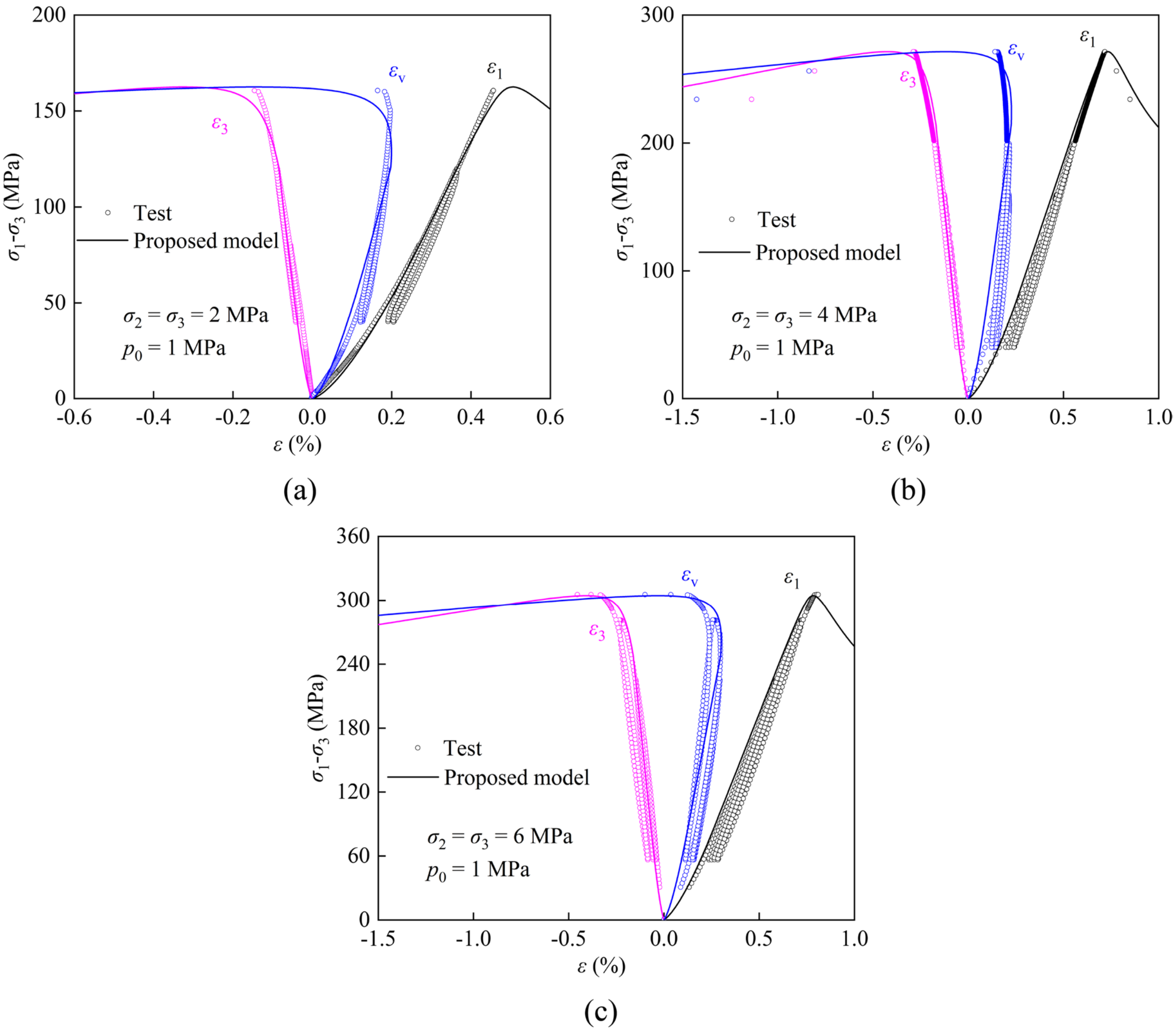

Fig. 16 Comparison of granitic gneiss stress–strain curves between the proposed model simulation results and triaxial cyclic loading and unloading hydro-mechanical test results under different σ_3 and the same p_0. **a** $p_0 = 1$ MPa, $\sigma_3 = 2$ MPa; **b** $p_0 = 1$ MPa, $\sigma_3 = 4$ MPa; **c** $p_0 = 1$ MPa, $\sigma_3 = 6$ MPa

Table 5 Peak strength comparison of granite gneiss between the proposed model simulation results and conventional triaxial hydro-mechanical coupling test results

σ_3 (MPa)	p_0 (MPa)	σ_p (MPa) (experiment)	σ_p (MPa) (model)
2	1	213.99	214.06
4	1	256.87	256.24
4	2	245.28	245.90
4	3	229.49	229.10
6	1	282.12	283.00

Table 6 Peak strength comparison of granite gneiss between the proposed model simulation results and triaxial cyclic loading and unloading hydro-mechanical coupling test results

σ_3 (MPa)	p_0 (MPa)	σ_p (MPa) (experiment)	σ_p (MPa) (model)
2	1	160.70	160.40
4	1	271.33	272.33
6	1	305.86	307.05

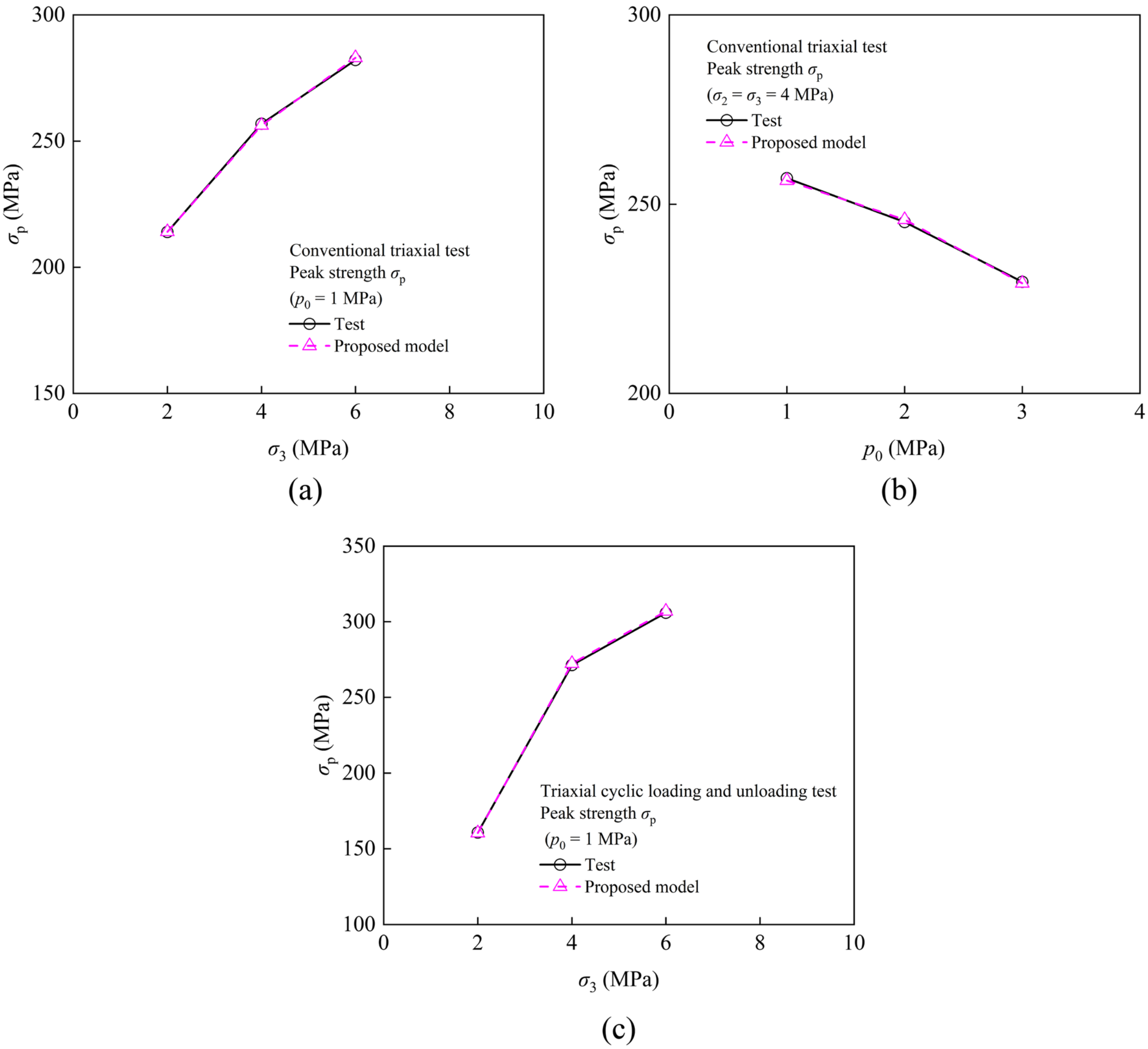

Fig. 17 Comparison of granite gneiss peak strength between the proposed model simulation results and hydro-mechanical coupling test results. Conventional triaxial test results. **a** at the same p_0 and different σ_3: $p_0=1$ MPa, $\sigma_3=2$, 4, 6 MPa; **b** at the same σ_3 and different p_0: $\sigma_3=4$ MPa, $p_0=1$, 2, 3 MPa; triaxial cyclic loading and unloading test results: **c** at the samep_0 and different σ_3: $p_0=1$ MPa, $\sigma_3=2$, 4, 6 MPa

$p_0=1$ MPa, $\sigma_3=1.5$, 3, 5, 7, 9 MPa; (2) $\sigma_3=5$ MPa, $p_0=0$, 1, 2, 3, 4, 4.5 MPa. Figure 18a shows the stress–strain curve prediction results for stress level (1); Fig. 18b shows the stress–strain curve prediction results for stress level (2). The prediction results show that the rock strength is linearly positively correlated with the effective confining stress (Fig. 19).

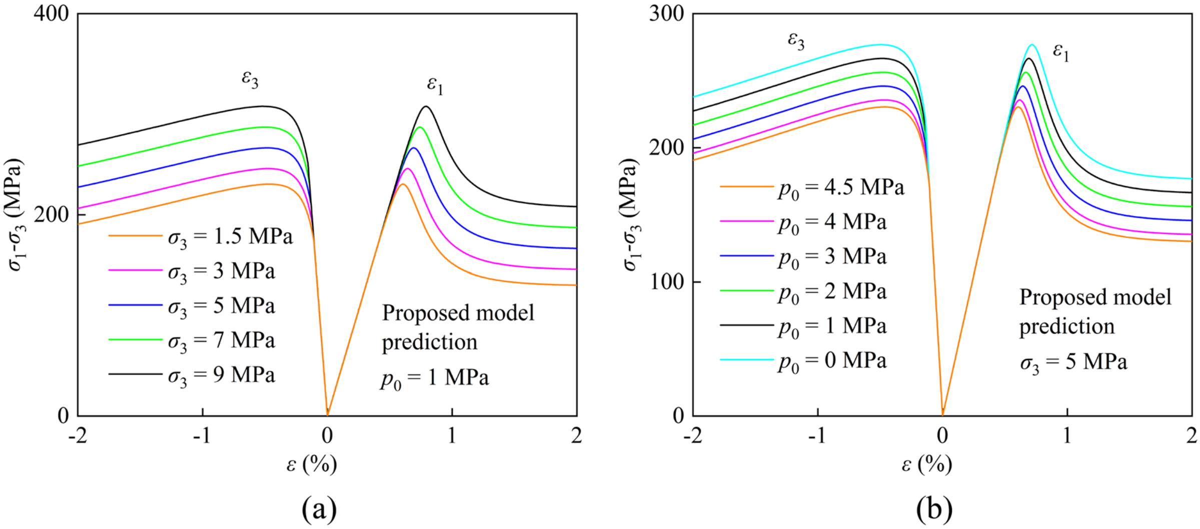

Fig. 18 The proposed model prediction of granitic gneiss stress–strain curve under untested stress levels. **a** at the same p_0 and different σ_3: $p_0 = 1$ MPa, $\sigma_3 = 1.5, 3, 5, 7, 9$ MPa; **b** at the same σ_3 and different p_0: $\sigma_3 = 5$ MPa, $p_0 = 0, 1, 2, 3, 4, 4.5$ MPa

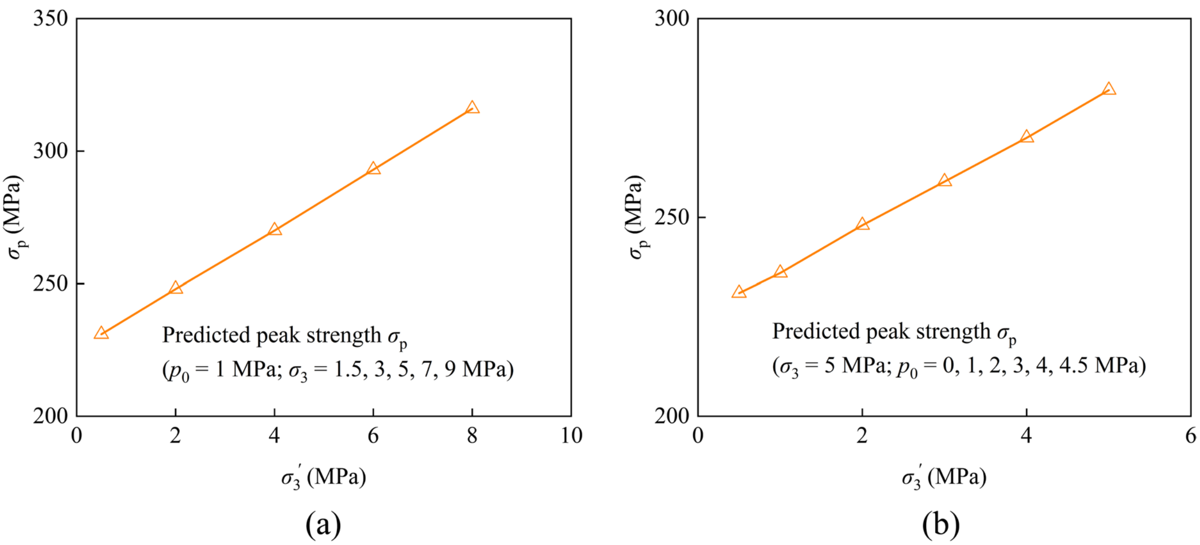

Fig. 19 Variation of granitic gneiss peak strength with effective confining pressure under untested stress levels. **a** at the same p_0 and different σ_3: $p_0 = 1$ MPa, $\sigma_3 = 1.5, 3, 5, 7, 9$ MPa; **b** at the same σ_3 and different p_0: $\sigma_3 = 5$ MPa, $p_0 = 0, 1, 2, 3, 4, 4.5$ MPa

7 Discussion

7.1 Verification and prediction of post-peak damage characteristics of rock under triaxial hydro-mechanical coupling conditions

The strength of rock after reaching the peak will not immediately drop to zero, but it shows certain post-peak nonlinear deformation characteristics. The nonlinear characteristics of rock under different effective confining pressures is different. With increasing effective confining pressure, the pre-peak hardening nonlinear characteristics of rock is more obvious, the post-peak softening rate is slower. According to the sensitivity analysis in Sect. 5.3, the pre-peak hardening and post-peak softening nonlinear behavior characteristics of

Table 7 Mechanical and model parameters of sandstone (Yu et al. 2019) under conventional triaxial hydro-mechanical coupling test

σ_3 (MPa)	p_0 (MPa)	E_0 (GPa)	υ	α	κ	h_1	h_0	ω_c	η	ζ	m
4	0.5								0.00010	80	4
6	0.5	14.60	0.27	0.44	6.80	1.10	0.70	0.8	0.00025	68	4
8	0.5								0.00060	55	12

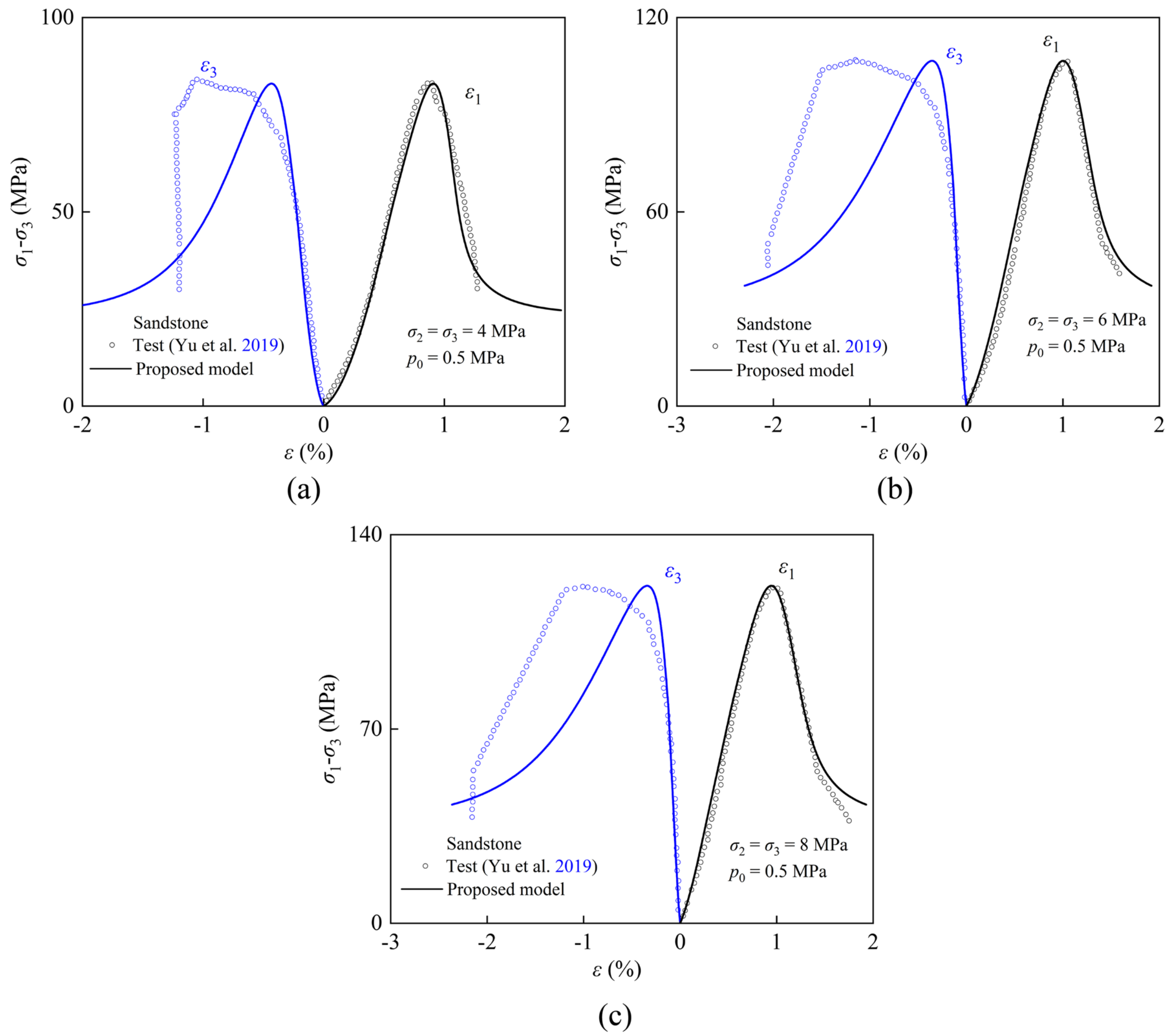

Fig. 20 Comparison of sandstone stress–strain curves between the proposed model simulation results and conventional triaxial hydro-mechanical coupling test results (Yu et al. 2019). **a** $\sigma_2=\sigma_3=4$ MPa, $p_0=0.5$ MPa; **b** $\sigma_2=\sigma_3=6$ MPa, $p_0=0.5$ MPa; **c** $\sigma_2=\sigma_3=8$ MPa, $p_0=0.5$ MPa

rock can be controlled by parameters η and ζ. Therefore, based on the conventional triaxial hydro-mechanical coupling test results of sandstone, which are cited from Yu et al. (2019), the parameters (Table 7) are determined according to the model parameter determination method in Sect. 5.2. The nonlinear characteristics of rock under different effective confining pressures can be better simulated by changing the parameters

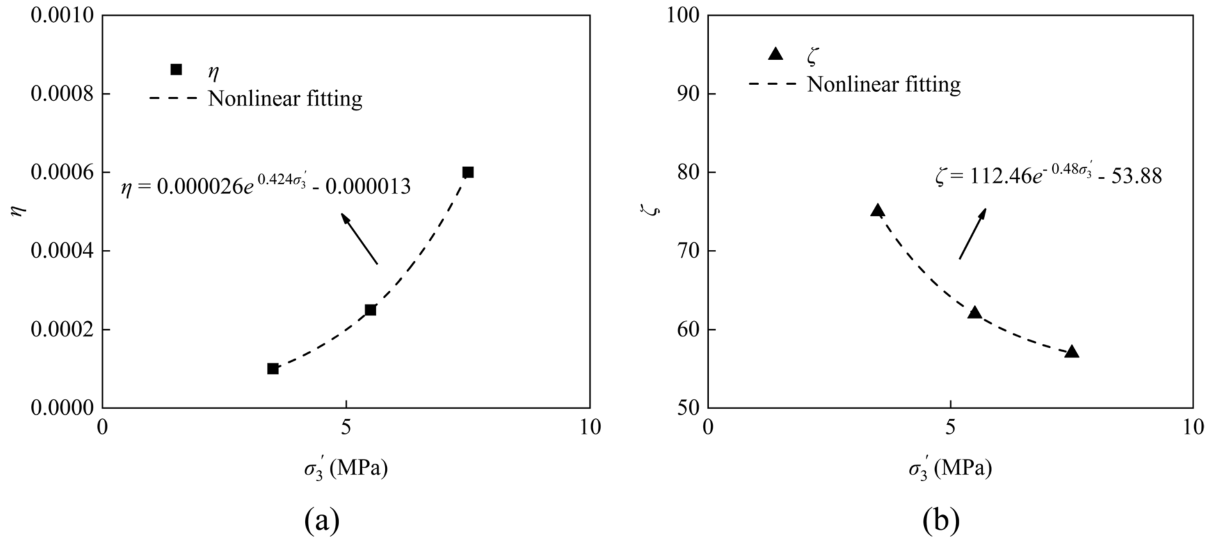

Fig. 21 The functions between the proposed model key parameters **a** η, **b** ζ and the effective stress

η and ζ, as shown in Fig. 20. There is a correlation between the key parameters (η and ζ) and the effective confining pressure, as shown in Fig. 21. According Eqs. (19) and (35), the functions of the key parameters (η and ζ) and the effective confining pressure can be fitted:

$$\eta(\sigma_3') = 0.000026e^{0.424\sigma_3'} - 0.000013 \tag{43}$$

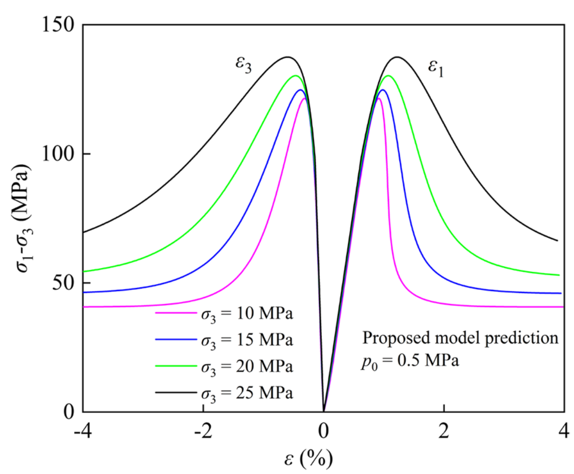

Fig. 22 The proposed model prediction of pre-peak hardening and post-peak softening behavior characteristics of rock under different effective confining pressures

$$\zeta(\sigma_3') = 112.46e^{-0.48\sigma_3'} + 53.88 \tag{44}$$

According to Eqs. (43) and (44), the difference in the pre- and post-peak nonlinear behaviors of rock under different effective confining pressures ($\sigma_3' = 9.5$, 14.5, 19.5, 24.5 MPa) can be further predicted, and the prediction result is shown in Fig. 22. With increasing effective confining pressure, the pre-peak nonlinear behavior of rock becomes more obvious, the post-peak softening rate decreases, and the post-peak stress decline rate slows down.

7.2 Verification and prediction of mechanical characteristics of rock under true triaxial hydro-mechanical coupling conditions

Deep rock has undergone complex stress redistribution, and there are not only conventional triaxial stress states ($\sigma_1 = \sigma_2 = \sigma_3$) but also true triaxial stress states ($\sigma_1 > \sigma_2 = \sigma_3$) inside rock. In this work, the proposed model can not only consider the influence of confining pressure on rock strength evolution but also consider the influence of intermediate principal stress on rock strength evolution. At present, there are few tests and models considering pore pressure under true triaxial stress. We summarize some true triaxial test results considering pore pressure (Li

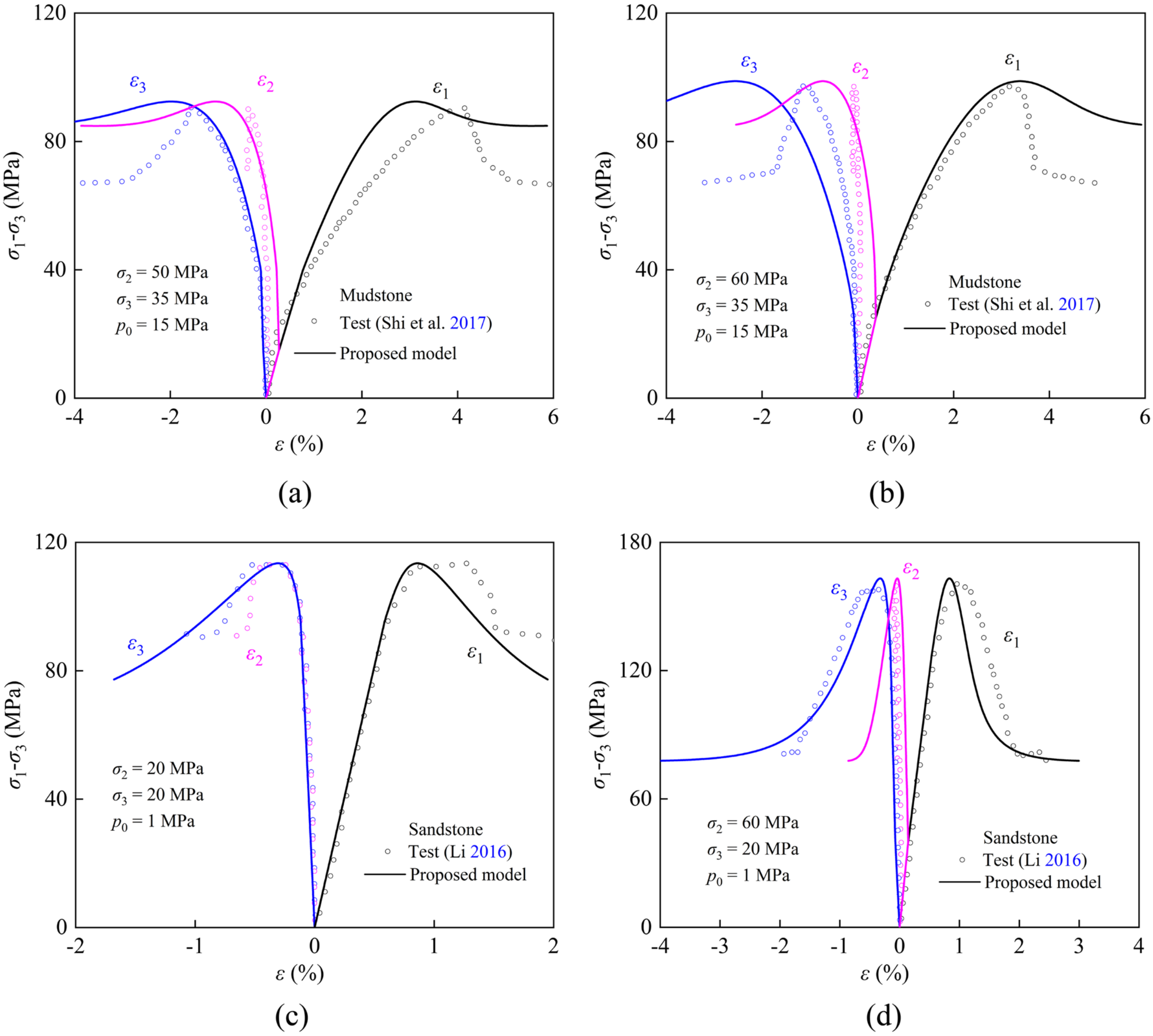

Fig. 23 Comparison of stress–strain curves between the proposed model simulation results and true triaxial hydro-mechanical coupling test results. **a** $\sigma_2 = 50$, $\sigma_3 = 35$ MPa, $p_0 = 15$ MPa; **b** $\sigma_2 = 60$, $\sigma_3 = 35$ MPa, $p_0 = 15$ MPa; **c** $\sigma_2 = 20$, $\sigma_3 = 20$ MPa, $p_0 = 1$ MPa; **d** $\sigma_2 = 60$, $\sigma_3 = 20$ MPa, $p_0 = 1$ MPa. Mudstone test results of **a** and **b** are cited from Shi et al. (2017); sandstone test results of **c** and **d** are cited from Li (2016)

Table 8 Mechanical and model parameters of mudstone (Shi et al. 2017) under true triaxial hydro-mechanical coupling test

σ_2 (MPa)	σ_3 (MPa)	p_0 (MPa)	E_0 (GPa)	υ	α	κ	h_1	h_0	ω_c	η	ζ	m
50	35	15	6.0	0.15	0.13	28.03	1.30	0.3	0.5	0.003	30	4
60	35	15										4

2016; Shi et al. 2017) to validate the proposed model, where the mudstone test results are cited from Shi et al. (2017), and the sandstone test results are cited from Li (2016). As shown in Fig. 23, the numerical simulation results with the proposed model are given, where the mechanical parameters and model parameters (Tables 8 and 9) are determined according to the method in Sect. 5.2. According to the comparison of the test and simulation results, the proposed model can well simulate the strength and deformation behaviors of rock under true triaxial stress.

Because there are very few true triaxial hydro-mechanical coupling tests at present and there is no test basis for determining key parameters, the pre- and post-peak nonlinear behaviors transition problem of rock caused by the change in effective stress is not considered temporarily. To study the mechanical behaviors of rocks under more complex stress conditions, based on the test results of Li (2016), the true triaxial compression stress–strain curve characteristics under different confining pressures and pore pressures ($\sigma_3 = 20$ MPa, $p_0 = 1$ MPa, $\sigma_2 = 30$, 40, 50, 70 MPa and $\sigma_2 = 60$ MPa, $\sigma_3 = 20$ MPa, $p_0 = 0$, 4, 8, 12, 16 MPa) are predicted, as shown in Fig. 24. In Fig. 24a, the rock strength increases with increasing σ_2, which is consistent with previous true triaxial test results for dry rock (Mogi 1973; Feng et al. 2019; Zheng et al. 2019, 2020); in Fig. 24b, the rock strength decreases with increasing p_0, which should be reasonable because the pore pressure reduces the effective stress resulting in a decrease in strength. In other words, the proposed model can better predict the strength characteristics of rocks under complex true triaxial stress levels.

Table 9 Mechanical and model parameters of sandstone (Li 2016) under true triaxial hydro-mechanical coupling test

σ_3 (MPa)	σ_3 (MPa)	p_0 (MPa)	E_0 (GPa)	υ	α	κ	h_1	h_0	ω_c	η	ζ	m
20	20	1	18.50	0.2	0.21	29.33	1.13	0.8	0.7	0.0005	70	14
60	20	1										14

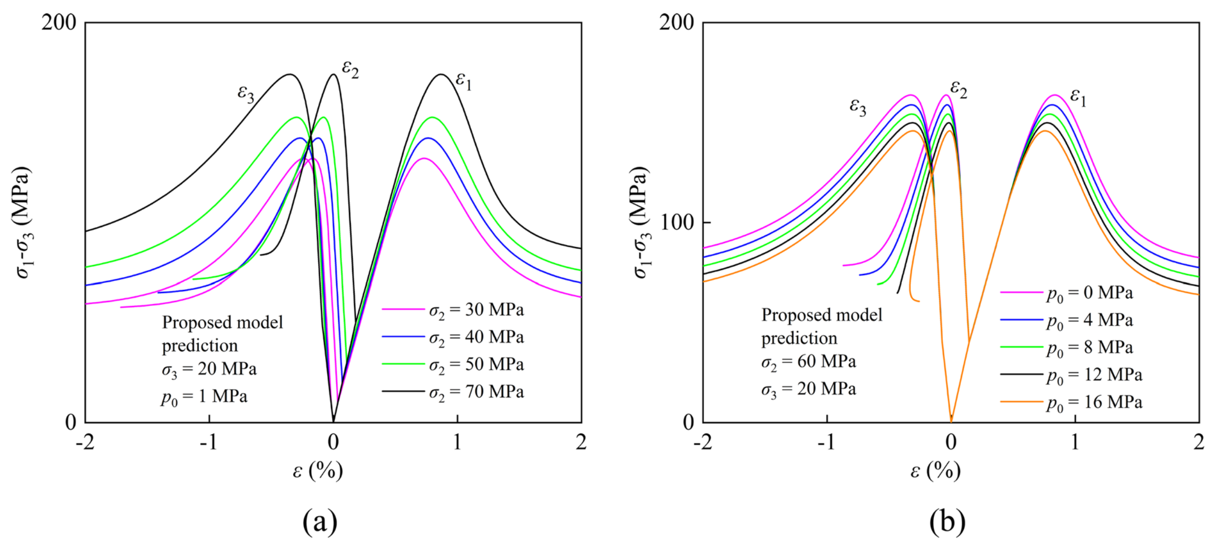

Fig. 24 The proposed model prediction of stress–strain curve characteristics of the proposed model under untested true triaxial stresses. **a** at the same σ_3, p_0 and different σ_2: $\sigma_3 = 20$ MPa, $p_0 = 1$ MPa, $\sigma_2 = 30$, 40, 50, 70 MPa; **b** at the same σ_2, σ_3 and different p_0: $\sigma_2 = 60$ MPa, $\sigma_3 = 20$ MPa, $p_0 = 0$, 4, 8, 12, 16 MPa

8 Conclusions

A series of triaxial compression and cyclic loading and unloading hydro-mechanical coupling tests were carried out for granite gneiss to investigate the stress–strain curves, strength and deformation characteristics under different confining pressures and pore pressures. Within the framework of irreversible thermodynamics, an elastic−plastic hydro-mechanical coupling damage constitutive model considering the compaction effect, pre-peak hardening and post-peak softening behaviors is established. The proposed model can simulate the mechanical characteristics of rock under different confining pressures and pore pressures. The main conclusions are as follows:

1. With decreasing confining pressure or increasing pore pressure, the peak strength and initial yield strength of granitic gneiss decrease. Under hydro-mechanical coupling conditions, the rock failure presents three stages of deformation characteristics: initial compaction, elastic deformation and nonlinear hardening, and confining pressure and pore pressure have a certain influence on it.
2. Within the framework of irreversible thermodynamics, an elastic−plastic hydro-mechanical coupling damage constitutive model, which can consider the compaction effect and describe the nonlinear behaviors of hardening and softening, is established. This model can better capture the evolution of the strength and deformation of granite gneiss under different confining pressures and pore pressures.
3. A compaction function C_{k} is introduced to reflect the change in the undamaged Young's modulus in the compaction stage to characterize the pre-peak compaction effect. The proposed model can better simulate the pre-peak and post-peak nonlinear behaviors of rock by the functional relationship between the key parameters (η and ζ) and the effective stress. The yield function of the proposed model considers the influence of intermediate principal stress and can be applied to the true triaxial stress states.

Acknowledgements The authors greatly acknowledge the financial support from the National Natural Science Foundation of China (Grant No. 52109119); the Guangxi Natural Science Foundation (Grant No. 2021GXNSFBA075030); the Open Research Fund of State Key Laboratory of Simulation and Regulation of Water Cycle in River Basin (China Institute of Water Resources and Hydropower Research) (Grant No. IWHR-SKL-202202); the Open Fund of Key Laboratory of Geological Hazards on Three Gorges Reservoir Area (China Three Gorges University), Ministry of Education (Grant No. 2022KDZ11); the Guangxi Science and Technology Project (Grant No. Guike AD20325002); the Systematic Project of Guangxi Key Laboratory of Disaster Prevention and Engineering Safety (Grant No. 2020ZDK007).

Author contributions ZZ: Conceptualization, Experiment, Methodology, Software, Writing–original draft. HS: Writing–original draft, Data curation, Software. WW: Writing–review and editing, Validation. ZW: Writing–review and editing, Software. ZL: Writing–review and editing, Supervision. BH: Writing–review and editing. GM: Data curation, Investigation. All authors read and approved the final manuscript.

Declarations

Competing interests The authors confirm that there are no known conflicts of interest associated with this publication and that there has been no significant financial support for this work that could have influenced its outcome.

References

Alejano LR, Bobet A (2012) Drucker–Prager criterion. Rock Mech Rock Eng 45:995–999. https://doi.org/10.1007/978-3-319-07713-0_22

Barton N (2002) Some new Q-value correlations to assist in site characterisation and tunnel design. Int J Rock Mech Min 39(2):185–216. https://doi.org/10.1016/S1365-1609(02)00011-4

Baud P, Schubnel A, Wong T (2000) Dilatancy, compaction, and failure mode in Solnhofen limestone. J Geophys Res Sol Earth 105(B8):19289–19303. https://doi.org/10.1029/2000JB900133

Bernabe Y (1986) The effective pressure law for permeability in Chelmsford granite and Barre granite. Int J Rock Mech Min 23(3):267–275. https://doi.org/10.1016/0148-9062(86)90972-1

Biot MA (1956) General solutions of the equation of elasticity and consolidation for a porous material. J Appl Phys 27:240–253. https://doi.org/10.1115/1.4011213

Braun P, Ghabezloo S, Delage P, Sulem J, Conil N (2019) Determination of multiple thermo-hydro-mechanical rock properties in a single transient experiment: application to shales. Rock Mech Rock Eng 52:2023–2038. https://doi.org/10.1007/s00603-018-1692-x

Cai M, Kaiser P, Tasaka Y, Maejima T, Morioka H, Minami M (2004) Generalized crack initiation and crack damage stress thresholds of brittle rock masses near underground excavations. Int J Rock Mech Min 41(5):833–847. https://doi.org/10.1016/j.ijrmms.2004.02.001

Caine JS, Evans JP, Forster CB (1996) Fault zone architecture and permeability structure. Geology 24(11):1025–1028. https://doi.org/10.1130/0091-7613(1996)024%3c1025:FZAAPS%3e2.3.CO;2

Chen L, Wang CP, Liu JF, Liu J, Wang J, Jia Y, Shao JF (2015) Damage and plastic deformation modeling of Beishan granite under compressive stress conditions. Rock Mech Rock Eng 48:1623–1633. https://doi.org/10.1007/s00603-014-0650-5

Fairhurst CE, Hudson JA (1999) Draft ISRM suggested method for the complete stress–strain curve for intact rock in uniaxial compression. Int J Rock Mech Min 36(3):281–289

Fang Z, Wu W (2022) Laboratory friction-permeability response of rock fractures: a review and new insights. Geomech Geophys Geo-Energy Geo-Resour 8:15. https://doi.org/10.1007/s40948-021-00316-8

Feng XT, Haimson B, Liu XC, Chang CD, Ma XD, Zhang XW, Ingraham M, Suzuki K (2019) ISRM suggested method: determining deformation and failure characteristics of rocks subjected to true triaxial compression. Rock Mech Rock Eng 52(6):2011–2020. https://doi.org/10.1007/s00603-019-01782-z

Giuffrida A, Agosta F, Rustichelli A, Panza E, Bruna VL, Eriksson M, Torrieri S, Giorgioni M (2019) Fracture stratigraphy and DFN modelling of tight carbonates, the case study of the Lower Cretaceous carbonates exposed at the Monte Alpi (Basilicata, Italy). Mar Petrol Geol 112:104045. https://doi.org/10.1016/j.marpetgeo.2019.104045

Guayacán-Carrillo LM, Ghabezloo S, Sulem J, Seyedi DM, Armand G (2017) Tunnel excavation in low-permeability anisotropic ground: effect of anisotropy and hydro-mechanical couplings on pore pressure evolution. Poromechanics VI: Proceedings of the sixth biot conference on poromechanics, pp 207–214. https://doi.org/10.1061/9780784480779.025

Hamiel Y, Lyakhovsky V, Agnon A (2004) Coupled evolution of damage and porosity in poroelastic media: theory and applications to deformation of porous rocks. Geophys J Int 156(3):701–713. https://doi.org/10.1111/j.1365-246X.2004.02172.x

Hoek E, Brown ET (2019) The Hoek–Brown failure criterion and GSI—2018 edition. J Rock Mech Geotech 11:445–463. https://doi.org/10.1016/j.jrmge.2018.08.001

Hu B, Zhang Z, Li J, Xiao H, Cui K (2022) Statistical damage model of rock based on compaction stage and post-peak shape under chemical-freezing-thawing-loading. J Mar Sci Eng 10:696. https://doi.org/10.3390/jmse10050696

Jia CJ, Zhang S, Xu WY (2021) Experimental investigation and numerical modeling of coupled elastoplastic damage and permeability of saturated hard rock. Rock Mech Rock Eng 54:1151–1169. https://doi.org/10.1007/s00603-020-02319-5

Katz AJ, Thompson AH (1986) Quantitative prediction of permeability in porous rock. Phys Rev B 34(11):8179. https://doi.org/10.1103/PhysRevB.34.8179

Khadijeh M, Yehya A, Maalouf E (2022) Propagation and geometry of multi-stage hydraulic fractures in anisotropic shales. Geomech Geophys Geo-Energy Geo-Resour 8:124. https://doi.org/10.1007/s40948-022-00425-y

Kou MM, Liu XR, Wang ZQ, Tang SD (2021) Laboratory investigations on failure, energy and permeability evolution of fissured rock-like materials under seepage pressures. Eng Fract Mech 247:107694. https://doi.org/10.1016/j.engfracmech.2021.107694

Laghaei M, Baghbanan A, Hashemolhosseini H, Dehghanipoodeh M (2018) Numerical determination of deformability and strength of 3D fractured rock mass. Int J Rock Mech Min 110:246–256. https://doi.org/10.1016/j.ijrmms.2018.07.015

Lemaitre A (1984) How to use damage mechanics. Nucl Eng Des 80(2):233–245. https://doi.org/10.1016/j.compgeo.2016.12.024

Li MH (2016) Research on multi-physics coupling behaviors of reservoir rocks under true triaxial stress conditions. College of Resource and Environmental Science of Chongqing University

Li W, Wang ZC, Qiao LP, Liu J, Yang JJ (2021) The effects of hydro-mechanical coupling on hydraulic properties of fractured rock mass in unidirectional and radial flow configurations. Geomech Geophys Geo-Energy Geo-Resour 7:87. https://doi.org/10.1007/s40948-021-00286-x

Liu HH, Chen HY, Han YH, Eichmann SL, Gupta A (2018) On the relationship between effective permeability and stress for unconventional rocks: analytical estimates from laboratory measurements. J Nat Gas Sci Eng 56:408–413. https://doi.org/10.1016/j.jngse.2018.06.026

Liu W, Zheng LG, Zhang ZH, Liu G, Wang ZL, Yang C (2021) A micromechanical hydro-mechanical-damage coupled model for layered rocks considering multi-scale structures. Int J Rock Mech Min 142:104715. https://doi.org/10.1016/j.ijrmms.2021.104715

Liu XS, Ning JG, Tan YL, Gu QH (2021b) Damage constitutive model based on energy dissipation for intact rock subjected to cyclic loading. Int J Rock Mech Min 85:27–32. https://doi.org/10.1016/j.ijrmms.2016.03.003

Liu Q, Zhao YL, Tang LM, Liao J, Wang XG, Tao Tan, Chang L, Luo SL, Wang M (2022) Mechanical characteristics of single cracked limestone in compression-shear fracture under hydro-mechanical coupling. Theor Appl Fract Mech 119:103371. https://doi.org/10.1016/j.tafmec.2022.103371

Lyakhovsky V, Shalev E, Panteleev I, Mubassarova V (2022) Compaction, strain, and stress anisotropy in porous rocks. Geomech Geophys Geo-Energy Geo-Resour 8:8. https://doi.org/10.1007/s40948-021-00323-9

Mitchell TM, Faulkner DR (2008) Experimental measurements of permeability evolution during triaxial compression of initially intact crystalline rocks and implications for fluid flow in fault zones. J Geophys Res-Sol Earth 113:B11. https://doi.org/10.1029/2008JB005588

Mogi K (1973) Rock fracture. Annu Rev Earth Pl Sci 1:63–84

Nakshatrala KB, Joodat SHS, Ballarini R (2018) Modeling flow in porous media with double porosity/permeability: mathematical model, properties, and analytical solutions. J Appl Mech 85:081009–1. https://doi.org/10.1115/1.4040116

Ning ZX, Xue YG, Li ZQ, Su MX, Kong FM, Bai CH (2022) Damage characteristics of granite under hydraulic and cyclic loading-unloading coupling condition. Rock Mech Rock Eng 55:1393–1410. https://doi.org/10.1007/s00603-021-02698-3

Putilov I, Kozyrev N, Demyanov V, Krivoshchekov S, Alexandr K (2022) Factoring in scale effect of core permeability at reservoir simulation modeling. SPE J 27:1930–1942. https://doi.org/10.2118/209614-PA

Rueda J, Mejia C, Noreña N, Roehl D (2021) A three-dimensional enhanced dual-porosity and dual-permeability approach for hydromechanical modeling of naturally fractured rocks. Int J Numer Methods Eng 112(7):1663–1686. https://doi.org/10.1002/nme.6594

Rutqvist J, Stephansson O (2003) The role of hydro-mechanical coupling in fractured rock engineering. Hydrogeol J 11:7–40. https://doi.org/10.1007/s10040-002-0241-5

Rutqvist J, Wu YS, Tsang CF, Bodvarsson G (2002) A modeling approach for analysis of coupled multiphase fluid flow, heat transfer, and deformation in fractured porous rock. Int J Rock Mech Min 39:429–442. https://doi.org/10.1016/S1365-1609(02)00022-9

Shao JF, Rudnicki JW (2000) A microcrack-based continuous damage model for brittle geomaterials. Mech Mater 32:607–619. https://doi.org/10.1016/S0167-6636(00)00024-7

Shao JF, Jia Y, Kondo D, Chiarelli AS (2006) A coupled elastoplastic damage model for semi-brittle materials and extension to unsaturated conditions. Mech Mater 38(3):218–232. https://doi.org/10.1016/j.mechmat.2005.07.002

Shen WQ, Liu SY, Xu WY, Shao JF (2022) An elastoplastic damage constitutive model for rock-like materials with a fractional plastic flow rule. Int J Rock Mech Min 156:105140. https://doi.org/10.1016/j.ijrmms.2022.105140

Shi L, Zeng ZJ, Bai B, Li XC (2017) Effect of the intermediate principal stress on the evolution of mudstone permeability under true triaxial compression. Greenh Gases 8(1):37–50. https://doi.org/10.1002/ghg.1732

Si XF, Gong FQ, Li XB, Wang SY, Luo S (2019) Dynamic Mohr–Coulomb and Hoek–Brown strength criteria of sandstone at high strain rates. Int J Rock Mech Min 115:48–59. https://doi.org/10.1016/j.ijrmms.2018.12.013

Simo JC, Taylor R (1986) A return mapping algorithm for plane stress elastoplasticity. Int J Numer Meth Eng 22(3):649–670. https://doi.org/10.1002/nme.1620220310

Tenthorey E, Stephen FC, Hilary FT (2003) Evolution of strength recovery and permeability during fluid–rock reaction in experimental fault zones. Earth Planet Sci Lett 206(1–2):161–172. https://doi.org/10.1016/S0012-821X(02)01082-8

Tian ZX, Zhang WS, Dai CQ, Zhang BL, Ni ZQ, Liu SJ (2019) Permeability model analysis of combined rock mass with different lithology. Arab J Geosci 12:755. https://doi.org/10.1007/s12517-019-4951-6

Wang JA, Park HD (2002) Fluid permeability of sedimentary rocks in a complete stress–strain process. Eng Geol 63(3–4):291–300. https://doi.org/10.1016/S0013-7952(01)00088-6

Wang ZC, Li W, Bi LP, Qiao LP, Liu RC, Liu J (2018) Estimation of the REV size and equivalent permeability coefcient of fractured rock masses with an emphasis on comparing the radial and unidirectional flow confgurations. Rock Mech Rock Eng 51:1457–1471. https://doi.org/10.1007/s00603-018-1422-4

Wang SS, Xu WY, Wang W (2020) Experimental and numerical investigations on hydro-mechanical properties of saturated fine-grained sandstone. Int J Rock Mech Min 127:104222. https://doi.org/10.1016/j.ijrmms.2020.104222

Wang SR, Liao HH, Chen YL, Fernández-Steeger TM, Du X, Xiong M, Liao SM (2021) Damage evolution constitutive behavior of rock in thermo-mechanical coupling processes. Materials 14(24):7840. https://doi.org/10.3390/ma14247840

Wen MJ, Xiong HR, Xu JM (2022) Thermo-hydro-mechanical response of a partially sealed circular tunnel in saturated rock under inner water pressure. Tunn Undergr Sp Tech 126:104552. https://doi.org/10.1016/j.tust.2022.104552

Wu N, Liang ZZ, Zhang ZH, Li SD, Lang YX (2022) Development and verification of three-dimensional equivalent discrete fracture network modelling based on the finite element method. Eng Geol 306:106759. https://doi.org/10.1016/j.enggeo.2022.106759

Xi X, Shipton ZK, Kendrick JE, Fraser-Harris A, Mouli-Castillo J, Edlmann K, McDermott CI, Yang ST (2022) Mixed-mode fracture modelling of the near–wellbore interaction between hydraulic fracture and natural fracture. Rock Mech Rock Eng 55:5433–5452. https://doi.org/10.1007/s00603-022-02922-8

Xia KZ, Chen CX, Wang TL, Zheng Y, Wang Y (2022) Estimating the geological strength index and disturbance factor in the Hoek–Brown criterion using the acoustic wave velocity in the rock mass. Eng Geol 306:106745. https://doi.org/10.1016/j.enggeo.2022.106745

Xiao WJ, Zhang DM, Li HT, Yu G, Yang H, Yu BC (2021) Difference analysis on sandstone permeability after treatment at different temperatures during the failure process: a case study of sandstone in Chongqing, China. Pure Appl Geophys 178:1893–1910. https://doi.org/10.1007/s00024-021-02740-z

Xu H, Prévost JH (2016) Integration of a continuum damage model for shale with the cutting plane algorithm.

Int J Numer Anal Met 41(4):471–487. https://doi.org/10.1002/nag.2563
Xue JH, Wang SL, Yang QL, Du YT, Hou ZX (2022) Study on damage characteristics of deep coal based on loading rate effect. Minerals 12(4):402. https://doi.org/10.3390/min12040402
Yang T, Liu HY, Tang CA (2017) Scale effect in macroscopic permeability of jointed rock mass using a coupled stress–damage–flow method. Eng Geol 228:121–136. https://doi.org/10.1016/j.enggeo.2017.07.009
Yang HQ, Liu JF, Luo C, Zhou XP (2018) An elastic–plastic damage model considering capillary effect for petrol–water saturated sandstone. Int J Damage Mech 27(10):1516–1550. https://doi.org/10.1177/1056789517734036
Yu J, Xu WY, Jia CJ, Wang RB, Wang HL (2019) Experimental measurement of permeability evolution in sandstone during hydrostatic compaction and triaxial deformation. B Eng Geol Environ 78(7):5269–5280. https://doi.org/10.1007/s10064-018-1425-0
Yu J, Yao W, Duan K, Liu XY, Zhu YL (2020) Experimental study and discrete element method modeling of compression and permeability behaviors of weakly anisotropic sandstones. Int J Rock Mech Min 134:104437. https://doi.org/10.1016/j.ijrmms.2020.104437
Zhang LY (2013) Aspects of rock permeability. Front Struct Civ Eng 7:102–116. https://doi.org/10.1007/s11709-013-0201-2
Zhang R, Jiang ZQ, Sun Q, Zhu SY (2013) The relationship between the deformation mechanism and permeability on brittle rock. Nat Hazards 66:1179–1187. https://doi.org/10.1007/s11069-012-0543-4
Zhang Q, Shao C, Wang HY, Jiang BS, Jiang YJ, Liu RC (2020) A fully coupled hydraulic-mechanical solution of a circular tunnel in strain-softening rock masses. Tunn Undergr Sp Technol 99:103375. https://doi.org/10.1016/j.tust.2020.103375
Zhang C, Ma CK, Chen QL, Liu HM, Wu SW, Pan ZK, Zhang L (2021) Influence of rock percentage on strength and permeability of tailing-waste rock mixtures. Bull Eng Geol Environ 80:399–411. https://doi.org/10.1007/s10064-020-01911-x
Zhao Y, Chen M (2006) Fully coupled dual-porosity model for anisotropic formations. Int J Rock Mech Min 43(7):1128–1133. https://doi.org/10.1016/j.ijrmms.2006.03.001
Zhao H, Zhou S, Zhang L (2019) A phenomenological modelling of rocks based on the influence of damage initiation. Environ Earth Sci 78:143. https://doi.org/10.1007/s12665-019-8172-9
Zhao YL, Liu Q, Zhang CS, Liao J, Lin H, Wang YX (2021) Coupled seepage-damage effect in fractured rock masses: model development and a case study. Int J Rock Mech Min 144:104822. https://doi.org/10.1016/j.ijrmms.2021.104822
Zheng JT, Zheng LG, Liu HH, Ju Y (2015) Relationships between permeability, porosity and effective stress for low-permeability sedimentary rock. Int J Rock Mech Min 78:304–318. https://doi.org/10.1016/j.ijrmms.2015.04.025
Zheng Z, Feng XT, Zhang XW, Zhao J, Yang CX (2019) Residual strength characteristics of CJPL marble under true triaxial compression. Rock Mech Rock Eng 52(4):1247–1256. https://doi.org/10.1007/s00603-018-1659-y
Zheng Z, Feng XT, Yang CX, Zhang XW, Li SJ, Qiu SL (2020) Post-peak deformation and failure behaviour of Jinping marble under true triaxial stresses. Eng Geol 265:1–12. https://doi.org/10.1016/j.enggeo.2019.105444
Zheng H, Cao SQ, Yuan W, Jaing Q, Li SJ, Feng GL (2022a) A time-dependent hydro-mechanical coupling model of reservoir sandstone during CO_2 geological storage. Rock Mech Rock Eng. https://doi.org/10.1007/s00603-022-02941-5
Zheng Z, Su GS, Jiang Q, Pan PZ, Huang XH, Jiang JQ (2022b) Mechanical behavior and failure mechanisms of cylindrical and prismatic rock specimens under various confining stresses. Int J Damage Mech 31(6):864–881. https://doi.org/10.1177/10567895221083997
Zheng Z, Su H, Mei GX, Cao YJ, Wang W, Feng GL, Jiang Q (2022c) Experimental and damage constitutive study of the stress-induced post-peak deformation and brittle–ductile behaviours of prismatic deeply buried marble. Bull Eng Geol Environ 81:427. https://doi.org/10.1007/s10064-022-02909-3
Zheng Z, Xu HY, Wang W, Mei GX, Liu ZB, Zheng H, Huang SL (2022d) Hydro-mechanical coupling characteristics and damage constitutive model of low-permeability granite under triaxial compression. Int J Damage Mech. https://doi.org/10.1177/10567895221132868
Zheng Z, Xu HY, He BG, Yang CX, Huang SL, Huang XH, Zhou JJ, Wang W (2022e) A new statistical damage model for true triaxial pre-and post-peak behaviors of rock considering intermediate principal stress and initial compaction effects. Int J Damage Mech. https://doi.org/10.1177/10567895221136161
Zheng Z, Cai ZY, Su GS, Huang SL, Wang W, Zhang Q, Wang YJ (2023a) A new fractional-order model for time-dependent damage of rock under true triaxial stresses. Int J Damage Mech 32(1):50–72. https://doi.org/10.1177/10567895221124325
Zheng Z, Su H, Mei GX, Wang W, Liu H, Zhang Q, Wang YJ (2023b) A thermodynamic damage model for 3D stress-induced mechanical characteristics and brittle–ductile transition of rock. Int J Damage Mech 32(4):623–648. https://doi.org/10.1177/10567895231160813
Zheng Z, Tang H, Zhang Q, Pan PZ, Zhang XW, Mei GX, Liu ZB, Wang W (2023c) True triaxial test and PFC3D-GBM simulation study on mechanical properties and fracture evolution mechanisms of rock under high stresses. Comput Geotech 154:105136. https://doi.org/10.1016/j.compgeo.2022.105136
Zhou GL, Tham LG, Lee PKK, Tsui Y (2001) A phenomenological constitutive model for rocks with shear failure mode. Int J Numer Anal Met 25(4):391–414. https://doi.org/10.1002/nag.135
Zhou ZL, Cai X, Ma D, Du XM, Chen L, Wang HQ, Zang HZ (2019) Water saturation effects on dynamic fracture behavior of sandstone. Int J Rock Mech Min 114:46–61. https://doi.org/10.1016/j.ijrmms.2018.12.014
Zhu WC, Tang CA (2004) Micromechanical model for simulating the fracture process of rock. Rock Mech Rock Eng 37(1):25–56. https://doi.org/10.1007/s00603-003-0014-z
Zhu ZN, Yang SQ, Ranjith PG, Tian H, Jiang GS, Dou B (2022) A statistical thermal damage constitutive model for

rock considering characteristics of the void compaction stage based on normal distribution. Bull Eng Geol Environ 81:306. https://doi.org/10.1007/s10064-022-02794-w